

SCANNING NEAR-FIELD INFRARED MICROSCOPY AND SPECTROMICROSCOPY APPLIED TO NANO-SYSTEMS AND CELLS

THÈSE N° 3296 (2005)

PRÉSENTÉE À LA FACULTÉ SCIENCES DE BASE

Institut de physique de la matière complexe

SECTION DE PHYSIQUE

ÉCOLE POLYTECHNIQUE FÉDÉRALE DE LAUSANNE

POUR L'OBTENTION DU GRADE DE DOCTEUR ÈS SCIENCES

PAR

Dušan VOBORNIK

DEA en microélectronique, Université Joseph Fourier, Grenoble, France
et de nationalité croate

acceptée sur proposition du jury:

Prof. G. Margaritondo, directeur de thèse
Prof. M. Chergui, rapporteur
Prof. A. Cricenti, rapporteur
Prof. N. H. Tolk, rapporteur

Lausanne, EPFL
2005

ABSTRACT	1
VERSION ABREGEE	3
1 SCANNING NEAR-FIELD OPTICAL MICROSCOPY (SNOM)	5
1.1 WHY SNOM?	5
1.1.1 Short History of Microscopy.....	6
1.1.2 The Resolution Limit of Lens-based Microscopes.....	7
1.1.3 New Microscopy Concepts and Techniques	11
1.1.4 SNOM vs. Other Microscopy Techniques	12
1.2 HISTORICAL DEVELOPMENT OF SNOM	14
1.3 APERTURE-BASED VS. APERTURELESS SNOM.....	15
1.4 APERTURE SNOM	18
1.4.1 Aperture SNOM Basics.....	18
1.4.2 Aperture SNOM Operation Modes: Collection and Illumination	20
1.4.3 Scanning.....	21
1.4.4 Light Transmission through a Sub-wavelength Size Aperture.....	25
REFERENCES	29
2 INFRARED SPECTROSCOPY SNOM EXPERIMENTS	31
2.1 WHY IR-SNOM?	31
2.2 INFRARED SPECTROSCOPY	33
2.3 IR-SNOM EXPERIMENTAL SETUP.....	35
2.3.1 Infrared SNOM Probe	36
2.3.2 Monochromatic, Tunable and Intense Infrared Source	38
2.3.3 Experimental Scheme.....	40
2.3.4 SNOM Instrument.....	41
2.3.5 Electronics.....	43
2.3.6 IR Detector.....	45
2.4 IR-SNOM IMAGING OF BORON NITRIDE FILMS.....	46
2.4.1 Boron Nitride (BN)	46
2.4.2 Laser Chemical Vapor Deposition (LCVD) of BN Films.....	47
2.4.3 BN Results	48
2.5 IR-SNOM STUDY OF LITHIUM FLUORIDE COLOR CENTERS.....	53
2.5.1 Lithium Fluoride (LiF) Color Centers.....	53
2.5.2 Colored LiF Pattern Preparation	53

2.5.3	LiF Results.....	54
2.6	IR-SNOM CELL IMAGING.....	56
2.6.1	Motivations.....	56
2.6.2	Targeting Specific Cell Constituents	57
2.6.3	Cell Preparation	59
2.6.4	Results	59
2.7	IR SIGNAL SUFFICIENCY	62
2.8	A REVIEW OF RECENT DEVELOPMENTS IN THE FIELD OF IR-SNOM.....	63
2.9	CONCLUSION.....	65
	REFERENCES.....	67
3	FLUORESCENCE SNOM IMAGING.....	73
3.1	INTRODUCTION.....	73
3.2	EXPERIMENTAL SETUP.....	75
3.3	IMAGING OF FLUORESCENTLY LABELED CELLS	77
3.4	CARBON NANOTUBES FLUORESCENCE IMAGING	80
3.4.1	Introduction	80
3.4.2	Experiment	81
3.5	CONCLUSION.....	83
	REFERENCES.....	85
	CONCLUSION.....	87
	ACKNOWLEDGMENTS.....	91
	CURRICULUM VITAE	93

Abstract

This thesis further explores the possibilities of scanning near-field optical microscopy (SNOM) in both materials and life sciences. Two experimental SNOM setups were developed: one designed for infrared spectroscopy applications and the other for the imaging of fluorescently labeled samples. The results of the experiments that were conducted with both setups are presented and analyzed in this thesis.

Diffraction limits the resolution of lens-based microscopes to a value close to that of the wavelength of the light that is used to illuminate the samples. SNOM instruments overcome this limit by probing the near-field light – the light that remains within close vicinity of the sample and decays exponentially away from it. The SNOM concept and instrumental design are described. A comparison of SNOM with other novel microscopies (electron, atomic force, and scanning tunneling microscopies) outlines the main advantages of SNOM – the sole *optical* microscopy technique with a nanometer resolution.

Aperture-based infrared SNOM (IR-SNOM), performed in the spectroscopic mode using the Vanderbilt University free electron laser, recently started delivering spatially resolved information on the distribution of chemical species and on other laterally fluctuating properties. The IR-SNOM combines the IR spectroscopy's chemical specificity and the SNOM's high optical and topographical resolutions. The IR-SNOM experimental setup is described in detail and results from the study of cells, boron nitride and lithium fluoride thin films are presented and analyzed. They demonstrate the great potential of this new technique. An overview of the development of IR-SNOM, as well as a consideration of its future possibilities are presented.

The newly built SNOM instrument at EPFL was used for experiments that are

complementary to the aforementioned IR-SNOM experiments. Specifically, the new SNOM enabled the study of fluorescently marked samples. Images of fluorescently labeled cells and carbon nanotubes are presented and analyzed. The results further demonstrate the exciting possibilities of SNOM.

Version Abrégée

Cette thèse explore les possibilités de la microscopie en champ proche optique à balayage (*scanning near-field optical microscopy* ou SNOM) dans la science des matériaux et science de la vie. Deux instruments ont été développés dans le cadre de ce travail : le SNOM combiné avec la spectroscopie infrarouge (IR-SNOM) et le SNOM pour l'imagerie des échantillons aux marqueurs fluorescents. Les résultats des expériences qui ont été effectuées avec ces instruments sont présentés et analysés dans cette thèse.

La résolution des microscopes classiques, basés sur l'utilisation des lentilles, est limitée par la diffraction, et sa valeur est du même ordre de grandeur que la longueur d'onde de la lumière utilisée pour illuminer l'échantillon. SNOM surmonte cette limite en sondant la lumière dans le champ proche de l'échantillon – la lumière qui ne se propage pas et dont l'intensité diminue exponentiellement avec la distance par rapport à l'échantillon. La comparaison du SNOM avec les autres nouvelles microscopies (microscopies électroniques, à force atomique, et à effet tunnel) souligne les avantages principaux du SNOM – la seule microscopie *optique* avec une résolution nanométrique.

Le SNOM à sonde à ouverture combiné à la lumière infrarouge (IR-SNOM) du laser à électrons libres de l'université Vanderbilt (Etats-Unis) et utilisé en mode spectroscopique, a commencé à livrer des informations sur la distribution latérale des espèces chimiques avec une résolution de l'ordre de 100 nm. Les expériences présentées dans cette thèse montrent le grand potentiel de cette nouvelle technique. Des échantillons comprenant des couches minces de nitrure de bore et de fluorure de lithium, ainsi que des cellules biologiques, ont été étudiés, et les résultats sont présentés et analysés. Une revue des développements du IR-SNOM est présentée et une vision de son essor futur est proposée.

Un nouveau SNOM a été construit à EPFL. L'instrument a été utilisé pour des expériences complémentaires à celles du IR-SNOM. Plus précisément, ce nouveau SNOM a servi à l'étude des échantillons aux marqueurs fluorescents. Des images de cellules biologiques et de nanotubes de carbone avec des marqueurs fluorescents sont montrées et analysées. Les résultats démontrent encore une fois les grandes possibilités de la microscopie en champ proche optique à balayage.

1 Scanning Near-field Optical Microscopy (SNOM)

Lens-based microscopes have a diffraction-limited resolution. Scanning Near-field Optical Microscopy instruments overcome this limit by probing the near-field light. A comparison of SNOM with other novel microscopies (electron, atomic force, and scanning tunneling microscopies) outlines the main advantages of SNOM – the sole *optical* microscopy technique with a nanometer resolution. Apertureless and aperture-based SNOM designs are debated, the latter being chosen for the experiments reported in this thesis because of its compatibility with fluorescence studies. The basics of the SNOM instrument design and mechanism, the light transmission through a sub-wavelength aperture and the importance of the probe shape, are discussed in detail.

1.1 Why SNOM?

An average human eye can see details as small as 0.07 mm in size. The ability to see the smaller details of matter is directly correlated with the development of science and our understanding of nature. Today's science needs *eyes* for the nano-world.

There is a great need, in fields such as biology, medical sciences and microelectronics, to determine shape, size, chemical composition, molecular structure and dynamic properties of nano-structures. To do this, microscopes with high spatial, spectral and temporal resolutions are required. Conventional, lens-based microscopes have the spatial resolution limited by diffraction. SNOM is a new step in the evolution of microscopy because its resolution is not subject to the diffraction limitation. SNOM offers up to 30 times better resolution* than conventional microscopy. It is the only *optical* microscopy method that can produce images with such a resolution.

1.1.1 Short History of Microscopy

The history of microscopy starts with the invention of lenses. Lenses are the base element of conventional microscopes. Lenses are pieces of transparent material (such as glass) that have two opposite surfaces curved (like a lentil, for example). There are reports of lenses having been used in ancient civilizations in China and Mesopotamia, but it is unclear whether they were used as jewelry or as optical instruments. The first written document describing the optical properties of lenses was authored by R. Bacon in 1267. There were several attempts to use lenses to make a microscope. It is A. Leeuwenhoeck who is most often acknowledged as the inventor of the microscope. In the 17th century he made a very simple instrument based on a single glass lens, which enabled him to discover bacteria, sperm cells and blood cells. Skilled at grinding lenses, he was able to build microscopes that magnified over 200 times. His contemporaries R. Hooke in England and J. Swammerdam in the Netherlands started building compound microscopes (i.e. microscopes using two or more lenses). These are conceptually similar to microscopes used today. The development of conventional microscopes continues today: attempts to perfect the shape of lenses, to build sophisticated combinations of

* Our experimental results, obtained with SNOM in combination with infrared light illumination; results, some of which are presented in chapter 2.

illumination and collection lenses, and the use of immersion objectives and confocal microscopes are just a few examples of the efforts to improve conventional microscopes.

1.1.2 The Resolution Limit of Lens-based Microscopes

The lateral resolution of an optical microscope is defined as the shortest distance between two points in an image of a specimen that can still be distinguished as separate entities. Some ambiguity in the use of the term “resolution” results from the variability in defining the distance that is sufficient to allow features to be distinguished as two objects rather than one. To define this distance, the so-called Rayleigh criterion is generally applied. The criterion states that two points are resolved in an image when the first minimum of the Airy (diffraction) pattern of one point is aligned with the central maximum of the diffraction pattern of the other point.

In the 1870s, German physicist Ernst Abbe worked for the Karl Zeiss company. His work is an early example of commercially funded research and development. At that time, microscopes were produced in an empirical way and their operational mechanism was not fully understood. Abbe’s aim was to establish serious scientific bases for the construction of microscopes. He demonstrated [1, 2], as would Lord Rayleigh shortly after him [3], that, due to the diffraction, lens-based microscopes are limited in their lateral resolution to:

$$D = 0.61 \frac{\lambda}{n \sin \theta} \quad (1.1)$$

In this equation, D is the shortest distance between two points on a specimen that can still be distinguished as separate entities, λ is the wavelength of the light producing the image, n the refractive index of the medium separating the specimen and the objective lens, and θ the aperture half-angle of the optical system. In practice, this means that the resolution achievable with the best (the most expensive) conventional

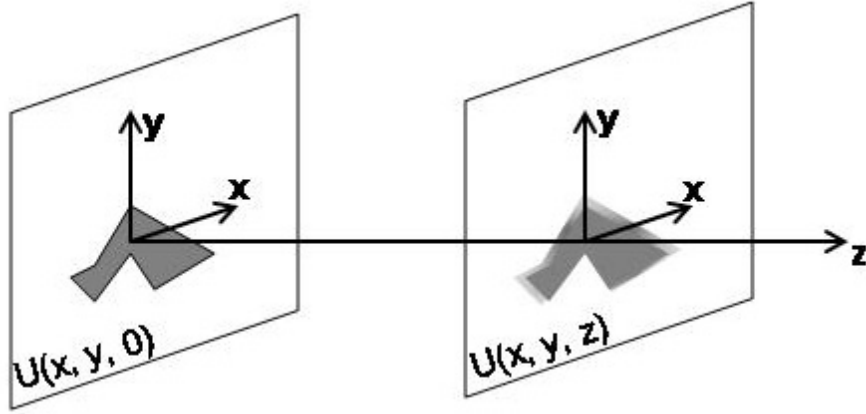


Figure 1-1: Optical image formation: field distribution at z due to the field at $z=0$.

microscopes is around 300 nm. This is a very frustrating limitation for the present-day science that tries to understand the nano-world. The most popular present-day research topic (nano-science) coincides with the resolution limit of conventional microscopy.

This limit, as well as the way to overcome it, can be understood using an analysis based on Fourier optics [4-8]. Consider an object in a plane $(x, y, 0)$ (see figure 1-1). Consider a plane wave \vec{E} incident on a transverse plane $(x, y, 0)$ propagating in the positive z direction. The 2-dimensional Fourier transform of the electric field in the plane of the object $(x, y, 0)$ is:

$$\vec{E}(f_x, f_y) = \int_{-\infty-\infty}^{+\infty+\infty} \vec{E}(x, y, 0) e^{-2\pi i(f_x x + f_y y)} dx dy \quad (1.2)$$

In this equation f_x and f_y are spatial frequencies of the plane structures, which can generally take any value between 0 and ∞ . Thus, $\vec{E}(x, y, 0)$ can be written as the inverse Fourier transform of its frequency spectrum:

$$\vec{E}(x, y, 0) = \int_{-\infty-\infty}^{+\infty+\infty} \vec{E}(f_x, f_y) e^{2\pi i(f_x x + f_y y)} df_x df_y \quad (1.3)$$

The field at the object can therefore be regarded as a superposition of plane waves propagating in the direction determined by the wave-vector:

$\vec{k} = (k_x, k_y, k_z) = (\alpha, \beta, \gamma) \frac{2\pi}{\lambda}$, with the direction cosines:

$$\alpha = \lambda f_x, \beta = \lambda f_y, \gamma = \sqrt{1 - \alpha^2 - \beta^2} \quad (1.4)$$

Similarly to equation 1.3, the electric field for $z > 0$ is given by:

$$\vec{E}(x, y, z) = \int_{-\infty-\infty}^{+\infty+\infty} \vec{E}(f_x, f_y, z) e^{2\pi i(f_x x + f_y y)} df_x df_y \quad (1.5)$$

In homogeneous, isotropic and linear media the \vec{E} field has to satisfy the Helmholtz equation $\nabla^2 \vec{E} + k^2 \vec{E} = 0$. Direct application of this requirement to equation 1.5 leads to the following solution:

$$\vec{E}(f_x, f_y, z) = \vec{E}(f_x, f_y) e^{2\pi i z \sqrt{\frac{1}{\lambda^2} - f_x^2 - f_y^2}} \quad (1.6)$$

In this equation, $k = 2\pi / \lambda$ is the magnitude of the wave-vector \vec{k} of the propagating wave. The combination of equations 1.6 and 1.5 gives the value of the electric field for $z > 0$:

$$\vec{E}(x, y, z) = \int_{-\infty-\infty}^{+\infty+\infty} \vec{E}(f_x, f_y) e^{2\pi i(f_x x + f_y y + z \sqrt{\frac{1}{\lambda^2} - f_x^2 - f_y^2})} df_x df_y \quad (1.7)$$

Two cases can be distinguished:

(1) $f_x^2 + f_y^2 < \frac{1}{\lambda^2}$: the argument of the exponential function in equation 1.6 is

imaginary, corresponding to a wave that propagates in the z direction towards the observation plane.

(2) $f_x^2 + f_y^2 > \frac{1}{\lambda^2}$: the equation 1.6 can be rewritten as:

$$\vec{E}(f_x, f_y, z) = \vec{E}(f_x, f_y) e^{-2\pi z \sqrt{f_x^2 + f_y^2 - \frac{1}{\lambda^2}}} \quad (1.8)$$

The argument of the exponential function in the equation 1.8 is real. As a consequence, the amplitude of the wave decreases exponentially in the z direction.

For low spatial frequencies, the waves propagate in the z direction towards the observation plane. These components are the *far-field* components of the angular frequency spectrum. The high spatial frequency components are only present near the sample and decay exponentially in the z direction. The region near the sample that contains the high spatial frequency components is called the near-field zone.

In conventional optical microscopy, lenses with a limited numerical aperture ($NA = n \sin\theta$) are placed in the far-field. Consequently, only waves propagating with their k -vector within the NA will reach the detector, which means that they fulfill the following condition:

$$\sin(\vec{z}, \vec{k}) < NA \quad (1.9)$$

By combining 1.4 and 1.9 we obtain the following equation:

$$\alpha^2 + \beta^2 < NA^2 \Rightarrow f_x^2 + f_y^2 < (NA/\lambda)^2 \Rightarrow \sqrt{\Delta x^2 + \Delta y^2} < \lambda / NA \quad (1.10)$$

This means that only spatial frequencies (f_x, f_y) smaller than NA/λ are detected, corresponding to lateral distances Δx and Δy in the plane $(x, y, 0)$ larger than λ/NA . As a result, the maximum achievable resolution in the image plane is limited to λ/NA ; this corresponds to the diffraction limit defined by Abbe [2]. Rayleigh also took into account a minimum contrast needed for the human eye to distinguish two features in an image. He defined the resolution limit as the distance between two points for which the first intensity maximum of the Airy (diffraction) pattern of the first point coincides with the first intensity minimum of the Airy pattern of the second point. The Rayleigh criterion corresponds to a contrast value of 26.4 percent. This has led to the generally quoted resolution limit of lens-based microscopes given by the equation 1.1 [3, 4].

Equation 1.8 reveals that waves containing the high spatial frequency information of the object do not propagate but decay exponentially away from the object. SNOM allows the detection of these non-propagating evanescent waves in the near-field zone, thus giving the high spatial frequency information about the object. To detect the evanescent light, a probe is brought into the near-field zone, close to the sample. It either detects the near-field light directly, or converts (by scattering) the evanescent waves into propagating waves so that these may be detected in the far-field. The probe is either a waveguide with a sub-wavelength-sized aperture or a nanometer-size scatter source.

1.1.3 New Microscopy Concepts and Techniques

Several new microscopy techniques were developed in the last century to overcome the resolution limit of conventional microscopes. The most successful are electron microscopy (Scanning Electron Microscope (SEM) and Transmission Electron Microscope (TEM)) and Scanning Probe Microscopy (SPM), which includes SNOM, Scanning Tunneling Microscope (STM) and Atomic Force Microscope (AFM).

There is an important conceptual difference between the electron microscopy and the SPM: electron microscopes work in a manner very similar to that of conventional microscopes. In electron microscopes, electrons play the same role photons play in conventional microscopy. They are focused and/or collected by magnetic or electrostatic lenses. Magnetic and electrostatic lenses have the same focusing effect with the electrons as the glass lenses have with the photons. Since electron microscopes use lenses, they are also subject to the diffraction limit: their resolution is defined by the same expression that is used to define the resolution of conventional microscopes (equation 1.1). The high resolution they achieve is due to the short relativistic wavelengths of the electrons.

SPM represents a real conceptual revolution in the way of observing an object: instead of putting a detector far from the sample and using the propagation of the physical quantity (photons, electrons, ions) to transfer information from the sample to the detector, the detector is set very close to the sample, in a so-called near-field zone. Here the notion of propagation becomes meaningless. Conventional microscopes use lenses to form magnified images of samples. SPM instruments do not use lenses; they operate with a very sharp probe that scans the sample, collecting signal point by point. The signal from each of these points becomes one pixel of the final image.

1.1.4 SNOM vs. Other Microscopy Techniques

There is a great need to determine shape, size, chemical composition, molecular structure and dynamic properties of nano-structures. To do this, microscopes with high spatial, spectral and temporal resolutions are required.

There are several microscopy techniques that have achieved technological maturity and are commercially available, widely used, and well understood by a larger scientific community. Conventional lens-based microscopy, SEM, TEM, AFM and STM are the best examples. The classical, lens-based optical microscope has a very good spectral and temporal resolution, but its spatial resolution is limited to more than half of the illumination wavelength (i.e. from 0.3 to 0.5 micrometers for visible light). Electron microscopes, STM and AFM easily achieve 10 nm or more in spatial resolution, but they perform poorly with respect to spectral and dynamic properties. Moreover, SEM, TEM and STM have to be operated in a vacuum and often require an extensive sample preparation, which limits their application in life sciences.

SNOM, on the other hand, is an optical microscopy technique. None of the other novel microscopy techniques is capable of gathering optical information (AFM, for example, allows sensing the shape of the sample, but not seeing it). SNOM produces

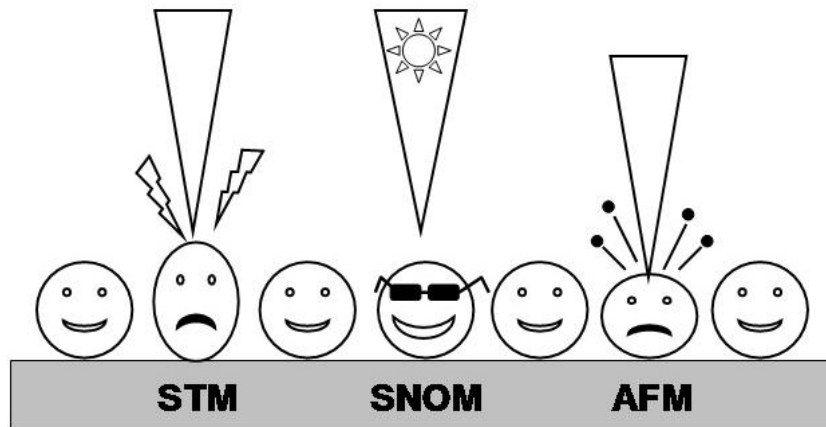


Figure 1-2: Humoristic comparison of SNOM with other scanning probe microscopy techniques, namely the Scanning Tunneling Microscopy (STM) and the Atomic Force Microscopy (AFM).

images with resolutions well beyond the diffraction limit. It allows the user to conduct spectroscopic studies with a lateral resolution reaching well into the sub-100 nm regime. It is a non-destructive and relatively inexpensive technique that does not require any particular sample preparation.

Yet, there are only a few companies that make commercially available SNOM instruments. This is not due to the novelty of the technique: SNOM was invented before the AFM. The complexity of the SNOM instrument makes it difficult to build one that would be easy to use for a non-expert.

In summary, SNOM offers a considerable advantage over other novel microscopy techniques because it is an *optical* technique with a resolution of a scanning probe microscopy. “Optical” means that SNOM can exploit the same contrast mechanisms that are used by the human eye. SNOM can be used in combination with spectroscopic methods as well as with all the techniques that were extensively developed for conventional microscopy, such as fluorescence labeling. SNOM is no longer an exotic method: it has matured into a valuable tool, ready to be applied to a large variety of problems in physics, chemistry and biology.

1.2 Historical Development of SNOM

The first to come up with the SNOM concept was Irish scientist E. Synge in 1928 [9]. He described an experimental scheme that would allow the optical resolution to extend into the nanometer regime without the use of lenses. He suggested the use of a strong light source behind a thin, opaque, metal film with a 100 nm diameter hole in it as a very small light source. He recommended that the aperture in the metal film be no further away from the sample than the aperture diameter (i.e. less than 100 nm). Images were to be recorded point by point by detecting the light transmitted through the sample by a sensitive photo-detector. The signal recorded at each point would be just one pixel of the final image. In 1932 he even proposed a way to scan the aperture at a few nanometers from the surface with great precision using piezo-electric actuators [10]. The proposed method is the main method used today in all scanning probe microscopy instruments. Unfortunately, Synge never turned his ideas into reality. His work was completely forgotten until uncovered by historian D. McMullan in the 1990s [11], well after the first SNOM instrument had appeared.

In 1956, J. O'Keefe described an experimental approach similar to that of Synge. In a short letter he presented a general idea on how to extend the optical microscopy resolution [12]. However, he did not propose any practical solutions on how to make such an instrument, unlike Synge whose work was much more elaborate. Yet, since Synge's ideas were forgotten, O'Keefe was often cited as the inventor of the SNOM concept.

Although Synge and O'Keefe developed the concept of SNOM, the first experimental demonstration of the validity of the concept had to wait until the 1970s. In 1972, Ash and Nichols described a microwave experiment that yielded scans widely cited as the first demonstration of near-field sub-wavelength imaging [13]. They imaged 0.5 mm wide lines of aluminum deposited on glass slides using electromagnetic radiation with a 3 cm wavelength. They achieved the resolution of $\lambda/60$ using microwaves and thus demonstrated that the SNOM concept is valid.

Another important step in the development of a practical SNOM instrument was the invention of a scanning tunneling microscope (STM) in IBM labs in Zurich in 1981. To manipulate the probe with a sub-nanometer precision the inventors G. Binnig and H. Rohrer used a scanner made of piezo-electric ceramic elements. Thus, in 1984, the nanometer-scale positioning technology became available, and an optical microscope similar to Syngé's proposed and forgotten scheme was re-invented by two separate groups: D. W. Pohl and his colleagues in the IBM labs in Zurich, Switzerland [14], and A. Lewis and his co-workers at Cornell University [15]. The Pohl and Lewis teams made the first SNOM instruments that worked with visible light (while Ash's and Nichols's demonstration was done with microwaves). This established a clear link between SNOM and conventional microscopy. The Zurich researchers called their microscope SNOM and those from Cornell called it NSOM. The two names are still in use today, which is often a cause for confusion because they both designate the exact same instrument. NSOM is mostly used by the North American scientific community and SNOM by the European one.

1.3 Aperture-based vs. Apertureless SNOM

Earlier in this chapter, equation 1.7 revealed that light waves containing the sample high spatial frequency information do not propagate and that their intensity decays exponentially as a function of the distance from the sample surface. These waves remain in the so-called near-field (less than one wavelength from the sample) and are called non-propagating or evanescent waves. There are two methods that allow the detection of these non-propagating waves, resulting in two distinct SNOM instrument designs: apertureless SNOM and aperture-based SNOM.

In apertureless SNOM [16, 17], the probe is a nanometer-size metal tip that is used as a scatter source. It is brought close to the sample (usually less than 10 nm from the surface) where it converts the evanescent waves into propagating waves by

scattering. These propagating waves, which originate in the near-field, are detected in the far-field.

In aperture SNOM the probe is a waveguide with a tapered tip that ends with a very small, sub-wavelength size aperture. The aperture is brought into the near-field zone (0-10 nm from the surface of the sample) where it collects the evanescent light and guides it through the waveguide to the detector.

Resolution-wise, the apertureless technique is better. It typically renders a resolution of around 10 nm. Ideally, apertureless SNOM uses an atomically sharp metallic probe (a probe tapered so sharply that its tip ends with a single atom), very similar to the STM or AFM probe. The probe scans the sample. During the scanning, the distance between the probe tip and the sample surface remains constant and very small (0-10 nm). The sample is illuminated from the far-field, for example by focusing a laser spot on the scanned zone around the probe's tip. The metallic probe further enhances the illumination field in an antenna-like manner or by surface plasmon field effects, and thus concentrates and amplifies the field at its tip. The enhanced field interacts with the sample and is scattered from the near-field zone by the tip. The detector is positioned in the far-field.

One of the main challenges in apertureless SNOM is to distinguish and take into account the light coming from under the tip only, since there is a relatively big surface of the sample around the tip that is also illuminated, giving rise to a strong background signal. One way to overcome this problem is to introduce a modulation of the tip/sample distance and to only take into account the signal that is modulated with the same frequency.

The success of the apertureless SNOM is due to the fact that present-day technology can produce atomically sharp tips. This means that an apertureless SNOM can, in principle, achieve atomic optical resolution!

Today, a typical resolution of an apertureless SNOM is somewhere between 5 and 30 nm, while the one of an aperture-based SNOM is between 50 and 150 nm. The limited resolution of the aperture-based SNOM is due to the fact that reducing the aperture diameter decreases the number of photons that can pass through the aperture. This in turn lowers the signal levels at the detector and decreases the signal-to-noise ratio, which imposes a conflicting limit on the resolution improvement that can be achieved by further reduction of aperture diameter.

Despite this, it is aperture-based SNOM which is presently the most widely used and developed near-field optical technique. All of the commercial instruments currently available use aperture probes. One of the reasons for this lies certainly in the fact that the aperture-based SNOM was the first to be developed in the mid 80s and the first apertureless SNOM experiments were presented later, in the mid 90s [16, 17].

There is another important advantage of the aperture-based setup that was particularly important for the researchers conducting the experiments reported in this thesis. Aperture is a very confined light source without any background light. This is in contrast to apertureless SNOM, where a rather large and intense laser spot is focused on a metallic nanometer-sized probe apex. In fluorescence SNOM applications this leads to the photo-bleaching of the entire illuminated zone around the tip, even before it can be scanned. In fluorescence experiments a localized illumination is extremely important. The application of the SNOM technique to biological problems is an essential part of this thesis, and fluorescence labeling and imaging is presently one of the main methods used in bio-research. We made a compromise and chose the SNOM approach that gives a slightly lower resolution, but that enables fluorescence imaging. All the work presented in this thesis was accomplished with an aperture-based SNOM.

1.4 Aperture SNOM

1.4.1 Aperture SNOM Basics

In the first SNOM experiment in 1984, Pohl et al. [14] used a metal-coated quartz tip, which was pressed against a surface to create an aperture. To create an image, the probe was put in contact with the sample at each pixel, and retracted when moved to the next pixel in order to avoid damaging the tip. Since this first experiment, both the near-field probe design and the scanning process have significantly improved. In 1991, Betzig et al. [18] introduced a SNOM probe made from a single-mode optical fiber. One end of the fiber is tapered to a tip size of approximately 50 nm. The taper is coated with aluminum. A sub-wavelength aperture is created in the aluminum coating at the tip of the taper (figure 1-3). Typical aperture diameters range from 30 to 150 nm. To keep the fiber in the near-field region of the sample, a distance regulation mechanism was implemented: the shear-force control [19, 20]. This mechanism enables keeping the aperture at a constant distance of a few nanometers from the sample surface while scanning.

Several other aperture SNOM probe designs and scanning mechanisms are used today. SNOM imaging can be performed, for example, with a SiO₂ tip integrated into an AFM Si cantilever; the tip is coated with metal and used for contact mode scanning [21]; bent optical fibers can be adapted for tapping mode SNOM [22]. The most common aperture SNOM setup, however, is based on straight optical fibers and shear-force scanning. This is also the technique that was used in this work. It is this SNOM setup that is described here.

Figure 1-3 illustrates the typical appearance of the tapered end of the optical fiber. The diameter of the aperture approximates the maximum resolution of the aperture SNOM. There are two methods that enable a routine production of 50-100 nm diameter apertures with optical fibers: the chemical etching and melting-pulling

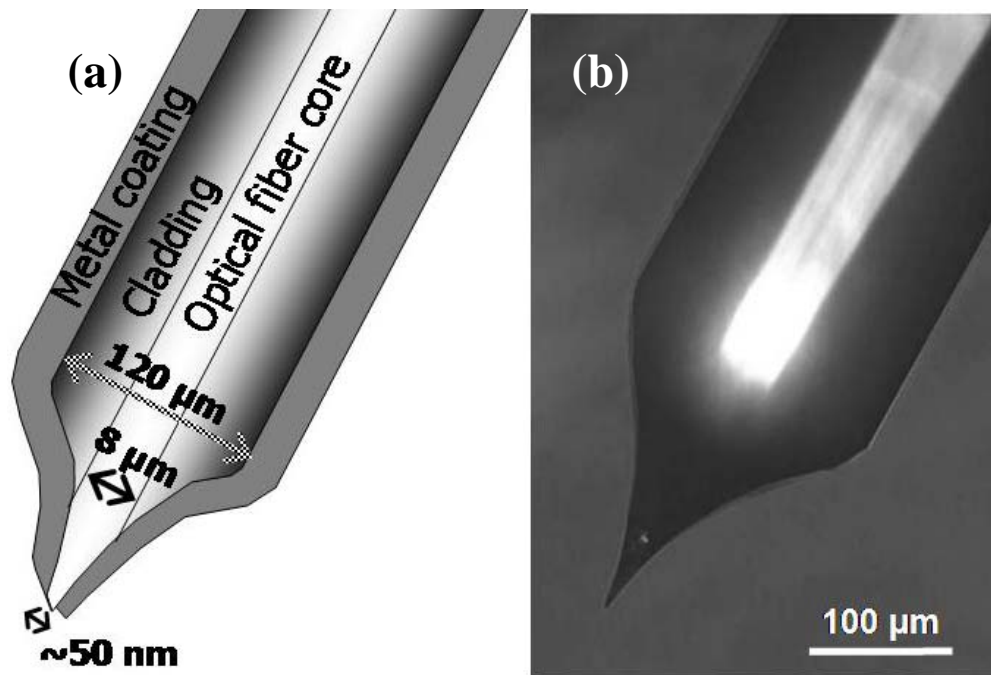


Figure 1-3: (a) Cross-section of the optical fiber's tapered end; (b) Photo of the optical fiber's tapered end as seen with a conventional microscope.

methods. Both of these methods were used in experiments reported in this thesis and will be described in the following chapters. The figure 1-3 (a) shows a cross-section of the fiber tip and indicates the most common dimensions of its core, cladding and aperture. A photo of the tapered end of a typical optical fiber used in the infrared SNOM experiments presented in this thesis is shown in the figure 1-3 (b).

The aperture has to be brought into the near-field zone, very close to the sample, to collect the light waves containing the high spatial frequency sample information (equation 1.7). Because of the exponential decay of the near-field waves, the probe has to be kept at a constant distance from the sample. Otherwise, the intensity changes caused by different probe-sample distances will shadow the desired contrast mechanisms (such as the absorption and reflection properties of the sample).

The aperture is scanned in a raster pattern over the surface of the sample while it either illuminates or collects the light from the sample surface (figure 1-4). During the scanning, the fiber tip has to be maintained at a constant distance of a few

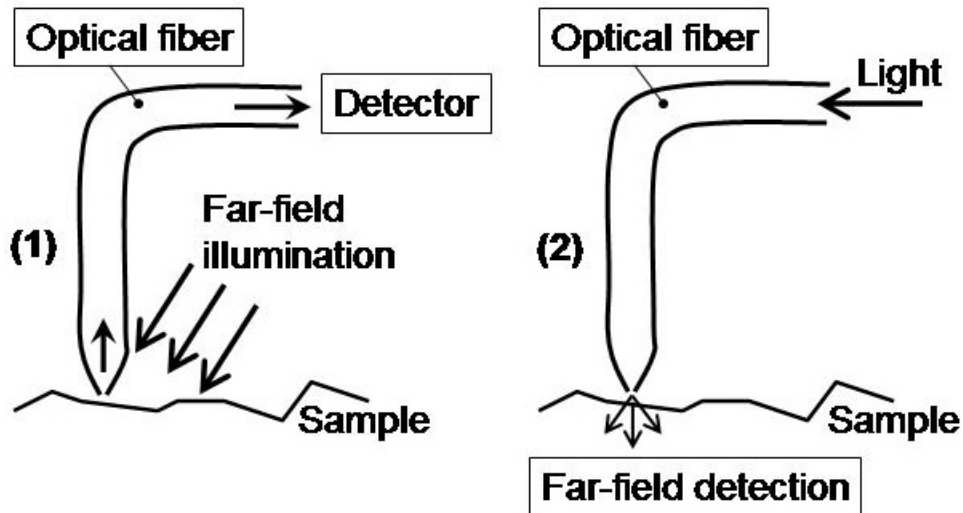


Figure 1-4: Basic aperture SNOM scheme. (1) Collection mode. (2) Illumination mode.

nanometers from the sample. In this way, the light is collected from (or illuminates) only a very small surface of the sample, which is under the aperture and which has approximately the same size as the aperture. As the aperture is scanned over the sample, the light signal is recorded point by point, using a suitable photo-detector. The total light intensity recorded from a certain point during scanning corresponds to only one pixel of the final image. In all the SNOM images shown in this thesis the lighter color corresponds to the higher intensity of the light signal.

1.4.2 Aperture SNOM Operation Modes: Collection and Illumination

There are three main SNOM operation modes, two of which are shown in the figure 1-4: (1) Collection mode: the sample is illuminated from the far-field (not through the fiber); this illumination gives rise to the evanescent light at the sample surface (in the near-field); the evanescent light is converted by the aperture into propagating waves inside the fiber, and conducted through the fiber to a suitable detector; (2) Illumination mode: the light is coupled into the fiber at its flat end, and conducted

through it to the tapered end, towards the aperture. The sub-wavelength aperture converts the propagating light into the evanescent field [23, 24]. The evanescent field interacts with the fine structure of the sample; this interaction converts the evanescent field into a propagating light wave, which is detected in the far-field. The third operation mode of the aperture-based SNOM is a combination of the two modes just mentioned. It is usually called the “illumination-collection” mode: the aperture is used both as the light source and as the collector. This operation mode requires a beam-splitter (for example a 2 x 2 fiber coupler) to separate the light that is directed to the sample from the light coming back from the sample and directed to the detector. Figure 1-4 illustrates the collection (1) and the illumination (2) modes. In each of these modes we can perform measurements both in transmission and in reflection. In the figure 1-4 the two combinations that were used in the experiments reported in this thesis are shown: on the left (1), the collection mode in combination with reflection (used in all our infrared SNOM measurements), and on the right (2), the illumination mode in combination with transmission (used in all our fluorescence SNOM experiments).

1.4.3 Scanning

The most important element of a SNOM instrument, besides the probe, is the scanning system. To get a nanometer resolution with SNOM, a nanometer resolution scanner is required. SNOM, STM and AFM use the same scanners. These scanners are made of piezo-electric materials, usually a PZT ceramic (Pb-Zr-Ti-O). Piezo ceramics are characterized by the fact that their dimensions change as a function of voltage applied to them, and vice-versa. Typically, several volts applied to a piezo ceramic scanner cause it to change a few nanometers in size. When the voltage is no longer applied, the ceramic goes back to its initial size. The size change is proportional to the value of the voltage applied. Thus, piezo ceramics are a perfect material for high precision actuators and scanners. Depending on the piezoelectric type and the scanner's size and design, the largest area that the scanner can cover is

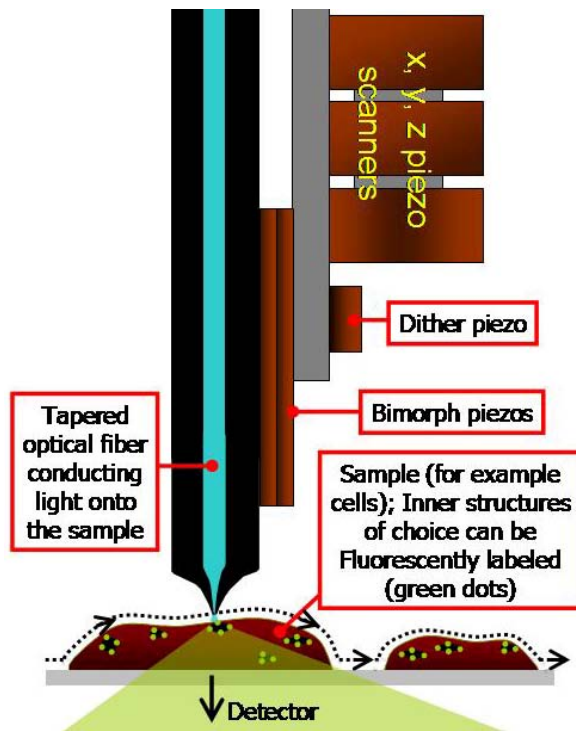


Figure 1-5: During the scanning, the SNOM fiber tip is maintained at a constant distance of less than 10 nm from the sample (dotted line). Arrows along the line show the scanning direction. Dots on the line correspond to the acquisition points.

usually several tens of microns. Commercially available scanners (see for example www.piezojena.com) can offer resolutions smaller than atomic diameters. These scanners usually contain three piezo blocs that move the SNOM tip in the x , y and z directions.

The most common SNOM feedback mechanism that controls the tip-to-sample distance is based on the so-called shear force [25]. The shear force is a short-range force and its intensity is significant only a few nanometers from the sample. The shear force feedback mechanism works in the following way: resonant lateral (x - y plane) oscillation of the

fiber tip is induced by applying an AC voltage to the dither piezo (see figure 1-5). The tapered end of the optical fiber is brought closer to the sample. When the tip of the fiber is at a few nanometers from the sample, the amplitude of the oscillation starts to be damped by shear forces (figure 1-6). The fiber tip is fixed to the bimorph piezo (see figure 1-5). The oscillation and bending of the fiber bends the bimorph piezo too. The bending piezo generates an AC voltage. The amplitude of the AC voltage is equivalent to the amplitude of the tip oscillation. Consequently, the amplitude of the oscillation of the tip can be monitored by monitoring the AC voltage from the bimorph piezo. This voltage is fed into a feedback loop, which then moves the tip in the z direction (towards and from the sample) in order to have a constant damped amplitude of the oscillation during scanning (typically, the best results are obtained with roughly 10 % damping). The distance between the fiber tip and the sample is kept constant by maintaining the damped amplitude of the

oscillation constant. Finally, the fiber tip is scanned laterally by x-y piezos, and the z piezo simultaneously moves it up and down in a way that maintains the distance between the aperture and the sample constant throughout the scanning.

The origin of the shear force is a controversial subject: first it was hypothesized that it is due to Van der Waals forces. Today, some experiments indicate that it is actually a viscous damping in a thin water layer confined between the tip and the sample (water originating from the ambient humidity) [26], and some indicate that the damping is caused by an

intermittent contact (where the tip actually knocks the sample during each of its oscillation) [27]. In SNOM applications, the topographic resolution is usually higher than the optical one, and seems much more limited by the size of the fiber probe than by the shear-force scanning mechanism. In some cases, when the sample contains regions that are physically very different (for example hydrophobic and hydrophilic regions) one must take into account possible shear-force scanning artifacts. Since the evanescent field decreases exponentially away from the sample surface, very small variations of the aperture-sample distance induce strong changes in the optical signal. Scanning artifacts also induce optical artifacts.

SNOM instruments produce two images simultaneously: the topography, similar to that given by a non contact AFM, is acquired at the same time as the optical image

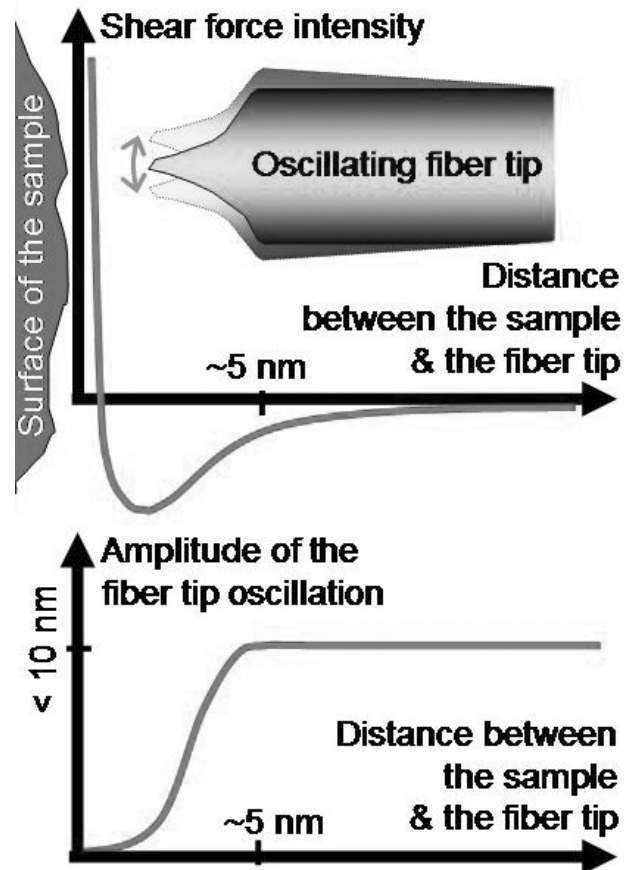


Figure 1-6: A typical shear force profile and its influence on the oscillation amplitude of an optical fiber SNOM tip, shown as a function of the distance separating the sample and the tip.

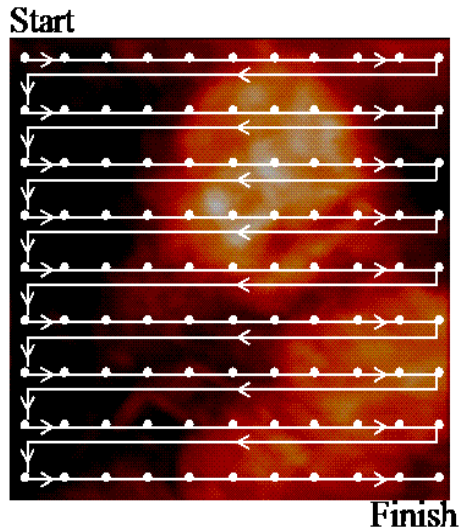


Figure 1-7: SNOM image of fluorescently labeled cells. Illustration of the signal acquisition: each of the white spots indicates a position where one pixel of the image is acquired. The white line shows the path of the fiber tip during scanning.

by recording movements of the z piezo. This additional capability of SNOM is extremely valuable: the two separate data sets (optical and topographical) can be compared to determine the correlation between the physical structures and the optical contrast.

The x - y - z scanner can either be attached to the specimen or to the optical fiber. Figure 1-5 illustrates a setup where the scanner is attached to the fiber. It is also very common to position a sample on the scanner, and scan it under the fiber tip. In this thesis both setups were used: in the infrared SNOM experiments the sample was fixed on the top of the scanner and scanned

under the fiber tip, and in the fluorescence SNOM applications it was the fiber that was attached to the scanner and scanned over the sample. Slight variations of the shear-force scanning system are used today. The one described here and illustrated in figure 1-5 is the scanning setup that was used for the fluorescence SNOM experiments discussed later in this thesis.

Figure 1-7 shows a typical scan path of a SNOM probe. The probe scans the sample line by line, point by point. It stops at an acquisition point (x - y movement), stabilizes its z position, the signal is recorded, and it moves to the next point. Users can choose several parameters: the size of the zone to scan, the density of the acquisition points, the scan velocity (the time the fiber takes to move from one point to another) are just some of the most common parameters that can be modified by the user. Shear-force scanning is a time-consuming technique: ideally, the fiber tip should make hundreds of oscillations when moving from one point to the other in order to detect very small shifts in the oscillation amplitude caused by topographic variations of the sample, and adapt the tip position correspondingly. That is why a compromise must be made between the scan size, the density of the acquisition points and the time for a single

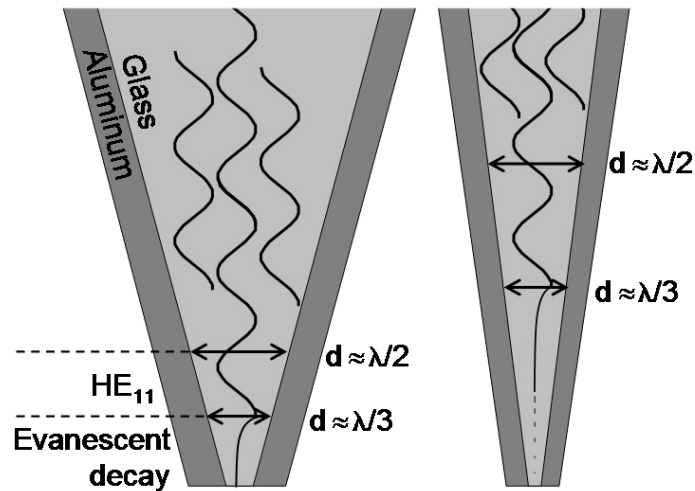


Figure 1-8: Schematized mode propagation in a SNOM probe. Cutoff diameters were calculated for the tapered aluminum-coated glass and the light wavelength $\lambda = 488$ nm [28].

scan to be completed. To get the highest resolution, one should choose the biggest number of points (thousands), but this would take hours with shear-force high resolution scanning. Consequently, the SNOM images that are most commonly found in the literature are 10 by 10 microns images with acquisition points every 25 to 50 nanometers.

1.4.4 Light Transmission through a Sub-wavelength Size Aperture

A typical light transmission of the aperture SNOM probe is very limited: only 10^{-3} - 10^{-6} of the light power coupled into the fiber is emitted by the aperture. The rest of the light is either back-reflected or absorbed by the coating in the taper region. The light transmission is determined by two factors: one is the taper cone angle and the other is the size of the aperture. Influence of the taper angle on the light throughput can be extrapolated from calculations presented in [28]: the efficiency of guiding light to the aperture is determined by the distribution of propagating modes in the tapered waveguide (even in single mode fibers, when the guiding core gets thinner in the taper, the guided mode spreads). The mode structure in a metallic waveguide is a function of the core (glass) diameter. This model shows that one mode after the other

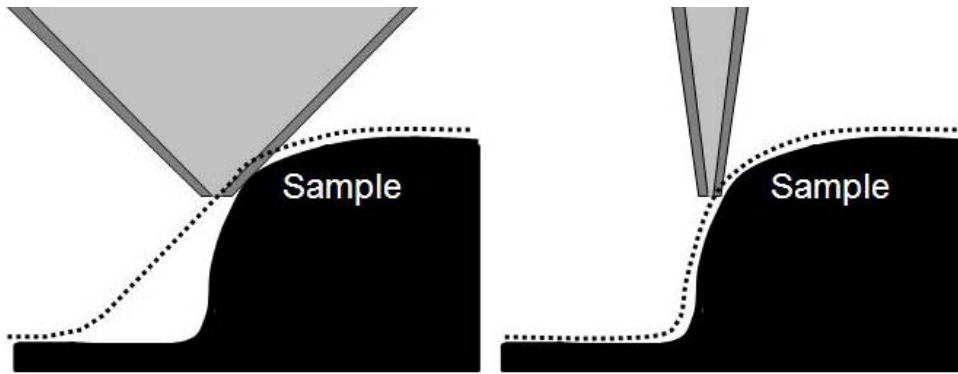


Figure 1-9: Topographic artifacts are induced when using SNOM probes with a bigger taper cone angle. Since the evanescent field detected by SNOM decreases exponentially away from the sample surface, these topographic artifacts also induce strong optical artifacts.

runs into cutoff when the core diameter gradually decreases. When the diameter of the glass becomes smaller than $\lambda/2$, only the HE_{11} mode still propagates (figure 1.8). Another cutoff occurs when the diameter becomes smaller than $\lambda/3$. Below this limit the HE_{11} mode becomes an evanescent wave. This means that the mode field decays exponentially [28, 29]. The amount of light that reaches the probe aperture depends on the distance separating the aperture and the $\lambda/3$ diameter section of the taper. This distance is smaller in tapers with larger cone angles (figure 1-8 on the left) than in those with smaller cone angles (figure 1-8 on the right).

The transmission coefficient of a sub-wavelength aperture in an infinitely thin and perfectly conducting screen has been calculated rigorously in [23] and [24]. This calculation predicts that the transmission coefficient is proportional to d^4/λ^4 , where d is the diameter of the aperture:

$$T \propto d^4/\lambda^4 \quad (1.11)$$

Transmission data were calculated for a realistic tip structure in [29] and extrapolated from [29] for different aperture diameters in [30] (calculations were done for the glass core with the aluminum cladding and the light wavelength $\lambda = 488$ nm). For a full taper cone angle of about 30° and a 100 nm aperture diameter, a transmission of

around 10^{-5} is expected. For a taper angle of about 42° the transmission values are around 10^{-3} . These values are in accordance with experimental results [31].

Working with very small apertures (< 40 nm diameter) is often impossible because the transmission coefficient decreases dramatically with decreasing aperture size (d^4/λ^4 law), leading to a signal-to-noise ratio that is insufficient in order to get reliable results. This cannot be by-passed by increasing the input light power because of the low damage threshold of the coating (≈ 10 mW). Large taper cone angles improve the transmission greatly, but this kind of probe is only suitable for very flat samples (figure 1-9).

The field distribution near the SNOM aperture depends strongly on the ratio d/λ (where d is the aperture diameter and λ the wavelength of the illumination light) [8, 29]. Basically, when d becomes smaller than λ , a part of the field that is transmitted through the aperture still propagates into the far-field, but the rest of the transmitted field remains strongly bound to the aperture and exponentially decreases away from it (it acts as an evanescent field). When the aperture is much smaller than the wavelength, the transmitted field is dominated by the evanescent components, and the far-field power emitted by the aperture strongly decreases.

Consider an aperture in the x - y plane and a propagating field arriving at the aperture in the positive z direction. The evanescent field E_z on the exit side of the aperture obeys the following equation:

$$E_z = C e^{-\frac{z}{\lambda}} \quad (1.12)$$

Where C is a constant depending on the refractive index of the medium before and after the aperture (usually glass and air) [8]. In common aperture SNOM experiments, this means that the light is strongly localized at the aperture. This strong localization of the field at the aperture is responsible for the resolution that can be achieved with SNOM [32]. SNOM is a surface selective technique: it is not the best instrument for studies of structures that are deeply imbedded below the sample

surface. Experimental studies performed on highly transparent samples (cells) indicate that structures more than 150 nm below the sample surface have negligible contributions to the observed signal [33].

The arguments presented in the section 1.4.4 were developed for the illumination mode of the aperture-based SNOM, where the illumination light propagates through the fiber and through the aperture onto the sample. However, since the Helmholtz equation cannot distinguish *up* from *down*, these results can also be applied to the collection mode SNOM, where the aperture collects the light from the sample surface, couples it into the fiber and guides it to the detector.

References

- [1] E. Abbe, *Archiv. Mikroskop. Anat.* **9**, 413-468 (1873)
- [2] E. Abbe, *J. Roy. Micr. Soc.* **2**, 300 and 460 (1882)
- [3] L. Rayleigh, *Philos. Mag.* **8**, 261-274 (1879)
- [4] M. Born, E. Wolf, *Principles of Optics*, Pergamon, Oxford (1987)
- [5] J. W. Goodman, *Introduction to Fourier Optics*, Mc Graw-Hill, New York (1968)
- [6] G. A. Massey, *Appl. Opt.* **23**, 658-660 (1984)
- [7] D. Courjon, C. Bainier, C. Girard, J. M. Vigoureux, *Ann. Physik* **2**, 149 (1993)
- [8] D. Courjon, *Near-Field Microscopy and Near-Field Optics*, Imperial College Press, London (2003)
- [9] E. H. Synge, *Philos. Mag.* **6**, 356-362 (1928)
- [10] E. H. Synge, *Philos. Mag.* **13(83)**, 297-300 (1932)
- [11] D. McMullan, *Proceedings RMS* **25**, 127-131 (1990)
- [12] J. A. O'Keefe, *J. Opt. Soc. Am.* **46**, 359 (1956)
- [13] E. A. Ash, G. Nichols, *Nature* **237**, 510-512 (1972)
- [14] D. W. Pohl, W. Denk, M. Lanz, *Appl. Phys. Lett.* **44(7)**, 651-653 (1984)
- [15] A. Lewis, M. Isaacson, A. Harootunian, A. Muray, *Ultramicroscopy* **13**, 227-232 (1984)
- [16] S. Kawata, Y. Inouye, *Ultramicroscopy*, **57**, 313-317 (1995)
- [17] F. Zenhausern, M. P. O'Boyle, H. K. Wickramasinghe, *Appl. Phys. Lett.* **65(13)**, 1623-1625 (1994)
- [18] E. Betzig, J. K. Trautmann, T. D. Harris, J. S. Weiner, R. S. Kostelak, *Science* **251**, 1468-1470 (1991)
- [19] E. Betzig, P.L. Finn and J.S. Weiner, *Appl. Phys. Lett.* **60**, 2484 (1992)
- [20] R. Toledo-Crow, P.C. Yang, Y. Chen and M. Vaez-Iravani, *Appl. Phys. Lett.* **60**, 2957 (1992)
- [21] L. Vaccaro, L. Aeschmann, U. Staufer, H. P. Herzog, R. Dändliker, *Appl. Phys. Lett.* **83**, 584-586 (2003)
- [22] A. Ianoul, M. Street, D. Grant, J. Pezacki, R. S. Taylor, L. J. Johnston, *Biophysical J.* **87**, 3525-3535 (2004)

- [23] H. Bethe, *Phys. Rev. (2)* **66**, 163-182 (1944)
- [24] C. J. Bouwkamp, *Philips Res. Rep.* **5**, 321-332 (1950)
- [25] E. Betzig, P. L. Finn, J. S. Weiner, *Appl. Phys. Lett.* **60**, 2484-2486 (1992)
- [26] R. Brunner, O. Marti, O. Hollricher, *J. Appl. Phys.* **86**, 7100-7106 (1999)
- [27] M. J. Gregor, P. G. Blome, J. Schöfer, R. G. Ulbrich, *Appl. Phys. Lett.* **68**, 307-309 (1996)
- [28] L. Novotny, C. Hafner, *Phys. Rev. E* **50**, 4094-4106 (1994)
- [29] B. Hecht, B. Sick, U. P. Wild, V. Deckert, R. Zenobi, O. J. F. Martin, D. W. Pohl, *J. Chem. Phys.* **112**, 7761-7774 (2000)
- [30] L. Novotny, D. Pohl, B. Hecht, *Opt. Lett.* **20**, 970-972 (1995)
- [31] D. Zeisel, S. Nettesheim, B. Dutoit, R. Zenobi, *Appl. Phys. Lett.* **68**, 2491-2492 (1996)
- [32] O. J. F. Martin, C. Girard, A. Dereux, *J. Opt. Soc. Am. A* **13**, 1801-1808 (1996)
- [33] A. Ianoul, M. Street, D. Grant, J. Pezacki, R. S. Taylor, L. J. Johnston, *Biophys. J.* **87**, 3525-3535 (2004)

2 Infrared Spectroscopy SNOM experiments

Recently, aperture-based infrared SNOM, performed in the spectroscopic mode using the Vanderbilt University free electron laser, started delivering spatially resolved information on the distribution of chemical species and on other laterally fluctuating properties. The practical examples presented here show the great potential of this new technique both in materials and life sciences. The IR-SNOM experimental setup is described in detail. Samples ranging from boron nitride and lithium fluoride thin films to cells were studied and the results are analyzed. The chapter ends with a discussion of the infrared SNOM perspectives.

2.1 *Why IR-SNOM?*

The infrared (IR) part of the electromagnetic spectrum is extremely interesting for spectroscopic investigations of matter [1, 2]. Since IR absorptions of molecular groups are highly specific, IR spectra show the chemical content of a sample.

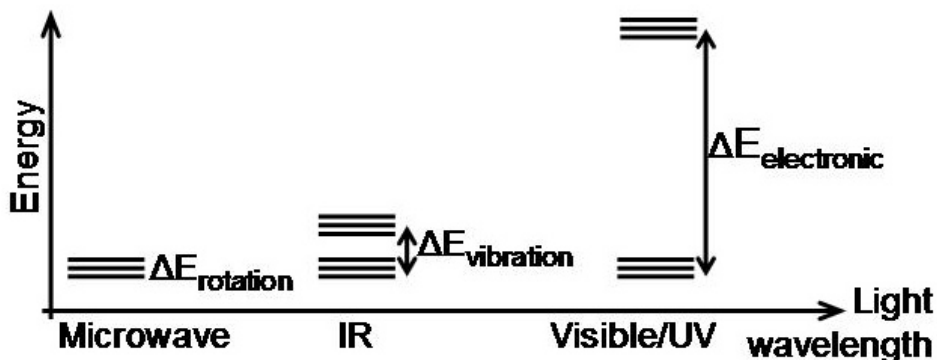


Figure 2-1: IR light energies are of the same order of magnitude as energies required for transitions to higher energy states of vibration of molecular bonds; microwaves' energies are equivalent to molecular-rotation energy transitions, while the visible and the UV light energies are sufficient for electronic energy-related transitions.

Microscopy with IR is particularly interesting as it enables users to produce chemical maps of the samples. These IR images allow one to see the spatial distribution of a specific molecule within a sample. This has led to the development of IR microscopes. Unfortunately, these microscopes have a very limited spatial resolution. IR microscopy is subject to the same resolution limitation as visible light microscopy, as defined by the equation 1.1 (Chapter 1, section 1.1.2). Equation 1.1 shows that the resolution is proportional to the wavelength of the illumination light. Since IR wavelengths are longer than the wavelengths of the visible light, the best resolution of commercial IR microscopes is generally of the order of $10\ \mu\text{m}$ [3]! This resolution limitation makes IR microscopes useless for present-day research hot-topics such as the study of cells and applications in microelectronics.

It was shown in the first chapter of this thesis that the resolution of SNOM instruments does not depend on the wavelength. The aperture-based SNOM resolution depends only on the size (diameter) of its aperture and on the separation between the sample and the aperture. In principle, the IR-SNOM can achieve the same resolution as the visible light-operated SNOM. Thus, combining SNOM and the IR would allow reducing the resolution limit from $10\ \mu\text{m}$, which is achievable with conventional IR microscopy, to $100\ \text{nm}$, which is routinely achievable with the aperture-based SNOM. This corresponds to a resolution gain of two orders of magnitude!

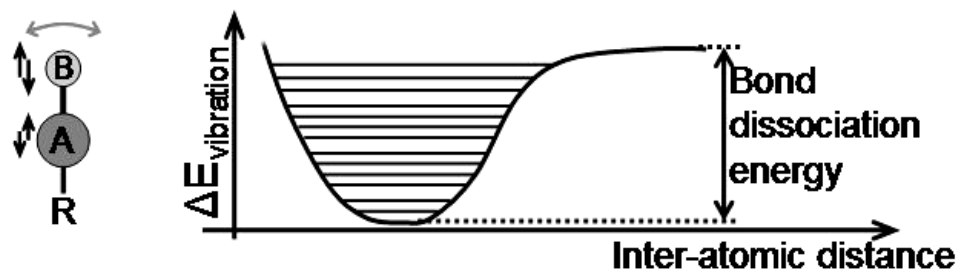


Figure 2-2: Vibration energy levels of a bond (A-B) and the related inter-atomic distance vibration range. The bond A-B can vibrate more or less independently of the rest of the molecule R. Vibrations can consist of stretching (illustrated by the black arrows on the left of A and B) or bond bending (illustrated by the gray arrow above B).

From a resolution point of view, the IR-SNOM imaging is even more exciting than that of the visible light-operated SNOM, since the gain in resolution, when compared with lens-based microscopy, is much higher. IR-SNOM imaging performed in a spectroscopic way can produce nanometer-resolved chemical maps of the sample and thus open an entire new field of research.

2.2 Infrared Spectroscopy

Infrared spectroscopy is a vibrational spectroscopy. Absorptions of the IR light correspond to excitations of vibrational modes of chemical bonds within molecules that compose the sample (see figures 2.1 and 2.2). The vibration energies are highly chemically specific: a given molecule absorbs only at specific wavelengths. The amount of light absorbed by the sample is measured while the wavelength is varied in order to obtain an IR spectrum.

Infrared radiation refers to the part of the electromagnetic spectrum between the visible light and microwaves. This broad region is commonly divided into three parts: near-IR (which corresponds to the radiation with a wavelength ranging from 710 nm to 2.5 μm), mid-IR (2.5 $\mu\text{m} < \lambda < 25 \mu\text{m}$) and the far-IR (25 $\mu\text{m} < \lambda < 1000 \mu\text{m}$). The region of the infrared spectrum that is of the greatest interest for spectroscopy is mid-IR, especially its wavelength range of between 2.5 and 10 μm .

Bond Type	Specific Context	Wave-numbers (cm ⁻¹) (Proportional to Vibration Frequencies)
C-H	C _{sp} 3-H	2800-3000
	C _{sp} 2-H	3000-3100
	C _{sp} -H	3300
C-C	C-C	1150-1250
	C=C	1600-1670
	C≡C	2100-2260
C-N	C-N	1030-1230
	C=N	1640-1690
	C≡N	2210-2260
C-O	C-O	1020-1275
	C=O of an amide	1640-1680 (6.1-5.9 μm)
	C=O of an ester	1730-1740

Table 2-1: IR chemical specificity: several C bonds and the wave-numbers of the IR radiation that they absorb.

The IR light from this spectral region excites molecular vibrations. To characterize the IR light, specialists usually use wave-numbers, in units of cm⁻¹, rather than the wavelength. The practical relationship between the light's wavelength and its wave-number is: Wave-number (in cm⁻¹) = 10000 / (λ (in μm)). Thus, the region between 2.5 and 10 μm wavelengths corresponds to wave-numbers between 4000 and 1000 cm⁻¹.

Although the IR spectrum is characteristic of the entire molecule, certain groups of atoms give rise to bands at around the same frequency regardless of the structure of the rest of the molecule. The wavelength of absorption depends on the relative masses of the atoms and the force constants of the bonds. There are two types of molecular vibrations: stretching and bending (see figure 2-2). The stretching vibration is a rhythmical movement along the bond axis that causes the inter-atomic distance to increase and decrease. A bending vibration consists of a rhythmical change of the bond angle. Only the vibrations that result in a rhythmical change in the dipole moment of the molecule are excited by the IR light. The alternating electric field, produced by the changing charge distribution that accompanies a vibration, couples the molecule vibration with the oscillating electric field of the electromagnetic radiation.

Since many bonds within a molecule can give rise to absorptions at their specific IR wavelengths, even a very simple molecule can have a complex IR spectrum. No two

molecules will give exactly the same IR spectrum. Present-day chemistry takes advantage of this specificity. Infrared spectroscopy is one of the core spectroscopic techniques used for obtaining chemical information from a wide range of samples. This has led to a huge implementation of the Fourier Transform Infra-Red spectrometers (FTIR) [4]. With FTIR, precise sample identification can usually be accomplished in seconds. But while it enables users to detect the presence of a specific molecule in the sample, it does not provide information on the precise location of the molecule nor on its spatial distribution. A SNOM study of the sample can tell us not only if the sample contains a specific molecule, but also its position within the sample. With SNOM we get a highly resolved chemical map of the sample.

When combined with microscopic sampling, IR spectroscopy is one of the most potent techniques available to the modern analytical chemist, allowing samples down to 10 μm to be chemically characterized. SNOM can further reduce this sampling size to a nanometer regime and allow chemical imaging with a 100 nm resolution.

2.3 IR-SNOM Experimental Setup

There are two experimental conditions to satisfy in order to perform spectroscopic IR-SNOM experiments: (1) Infrared spectroscopic measurements require a tunable, monochromatic and intense IR source; (2) High quality IR fibers must be made and tapered into probes (Aperture-based SNOM instruments that work with visible light use probes made of standard telecommunications' silica optical fibers. These fibers exhibit strong absorptions in the mid-IR spectral region and are therefore unsuitable for the IR-SNOM).

Establishing collaborations with experts enabled us to satisfy the two conditions and to successfully perform spectroscopic IR-SNOM experiments with a variety of samples.

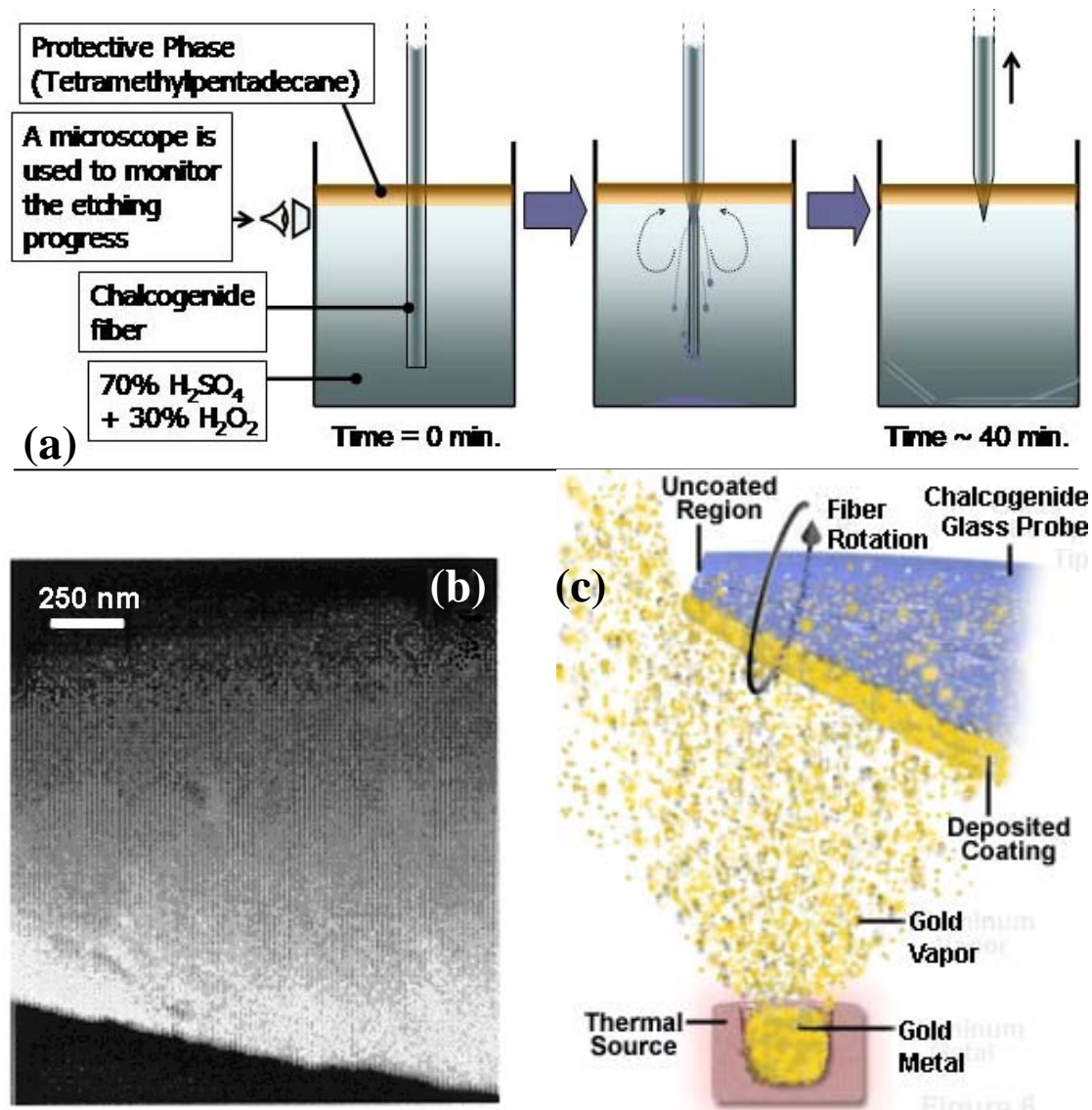


Figure 2-3: IR-SNOM probe fabrication. (a) Chemical etching of arsenic-sulfide fiber using a protective layer system. (b) SEM image of etched arsenic-sulfide taper shows its smooth surface. (c) A SNOM aperture is created by evaporating gold on a rotating taper with an angle of 25-30° between the fiber and the evaporator axis.

2.3.1 Infrared SNOM Probe

The fabrication of extremely high quality infrared fiber tips is a crucial technical step in the practical realization of IR-SNOM experiments. Chalcogenide glasses and optical fibers have a wide variety of applications because of their unique infrared

transmission in the 2 - 12 μm wavelength region [5]. Chalcogenide glasses are based on the chalcogen elements S, Se and Te (elements of the group 16 – old-style VIB or VIA – in the periodic table); the addition of other elements such as Ge, As and Sb, leads to the formation of stable glasses. We tested several types of chalcogenide fibers for IR-SNOM applications [7] and finally chose arsenic-selenide fibers. These fibers are good waveguides of IR in the wavelength range 3 - 11 μm [8].

Tapered IR-SNOM probes are obtained from single-mode, one meter long arsenic-selenide fibers with a 70 μm clad thickness and a 120 μm core diameter (see figure 2-4) [7]. Several methods have been proposed on how to prepare the tapered glass for SNOM probes. The most popular method is the adiabatic pulling of optical fibers while melting them with a CO_2 laser [9]. However, this method cannot be used for the IR fibers since they are transparent to the light emitted by CO_2 lasers. A convenient method consists of etching glass fibers at the meniscus between the etching solution and the protective over-layer (Turner method) [10]. A taper is formed due to a decreasing meniscus height as the fiber diameter is reduced by the etching solution. A piranha solution (7:3 ratio of $\text{H}_2\text{O}_2\text{:H}_2\text{SO}_4$) is used to etch, while tetra-methyl-penta-decane forms the protective layer. One end of the fiber is put into the solution. The etching typically takes 30 - 45 minutes, depending on the fiber diameter, etching concentration, and temperature. A conventional microscope is used to monitor the etching process in real time (see figure 2-3a).

An SMA adapter is fitted on the other end of the fiber using phenyl-salicylate as a solid support. Lubricated with water, the adapter end of the fiber is polished to a smooth clean surface using rotating aluminum oxide discs. The final polish is done with a 0.3 μm disc. This end of the fiber is interfaced with the detector during experiments.

The etched tips are coated with gold using a Varian thermal deposition system at a pressure of 10^{-6} Torr. The tips are held at a 25° - 30° angle above the evaporation point source to create an aperture (see figure 2-3c). In this way the very end of the tip

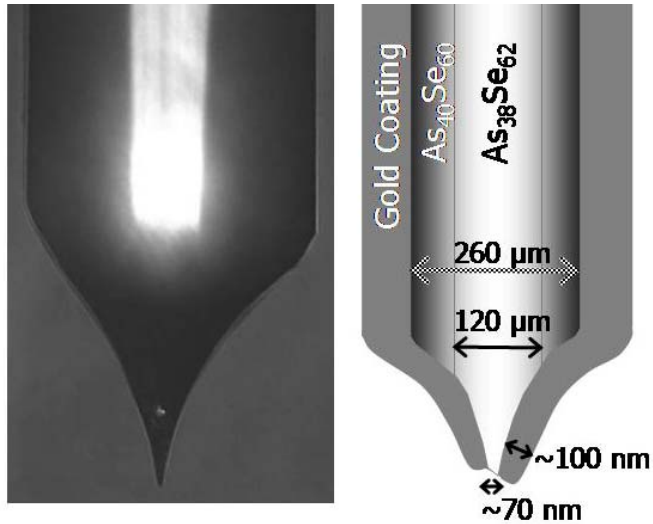


Figure 2-4: Chalcogenide optical fibers are good mid-IR waveguides. Right: section of a fiber tip ready for IR-SNOM use. Left: photo of an actual fiber tip we used in our experiments.

is not exposed to the gold gas flux. Tips are rotated during deposition to achieve a uniform gold coating. The thickness of the coating is 100-125 nm [7]. A well-known problem of etched tips is a rough glass surface [11]. This roughness is responsible for pinholes in the subsequently applied metal coating. SEM images of our tips show a smooth probe surface, without any holes in the coating that could lead to a

light transmission elsewhere than through the aperture (figure 2-3b). A ready-for-use chalcogenide fiber probe is shown in figure 2-4.

The main part of the work on IR-SNOM probes was done by our collaborators from the Naval Research Laboratory in Washington, DC (J. S. Sanghera, et al.). Today, chalcogenide optical fibers are also commercially available [12].

2.3.2 Monochromatic, Tunable and Intense Infrared Source

Another key technical problem in spectroscopic IR-SNOM is the need for the IR source to be monochromatic and tunable over a broad range of wavelengths. Equation 1.11 in the first chapter shows that the transmission coefficient of the SNOM aperture is proportional to d^4/λ^4 , where d is the diameter of the aperture and λ the wavelength of the light. Thus, the IR sub-wavelength aperture transmission is even more limited than the aperture transmission of the visible light. Hence, IR-SNOM also requires an intense IR source to offset the limited transmission.

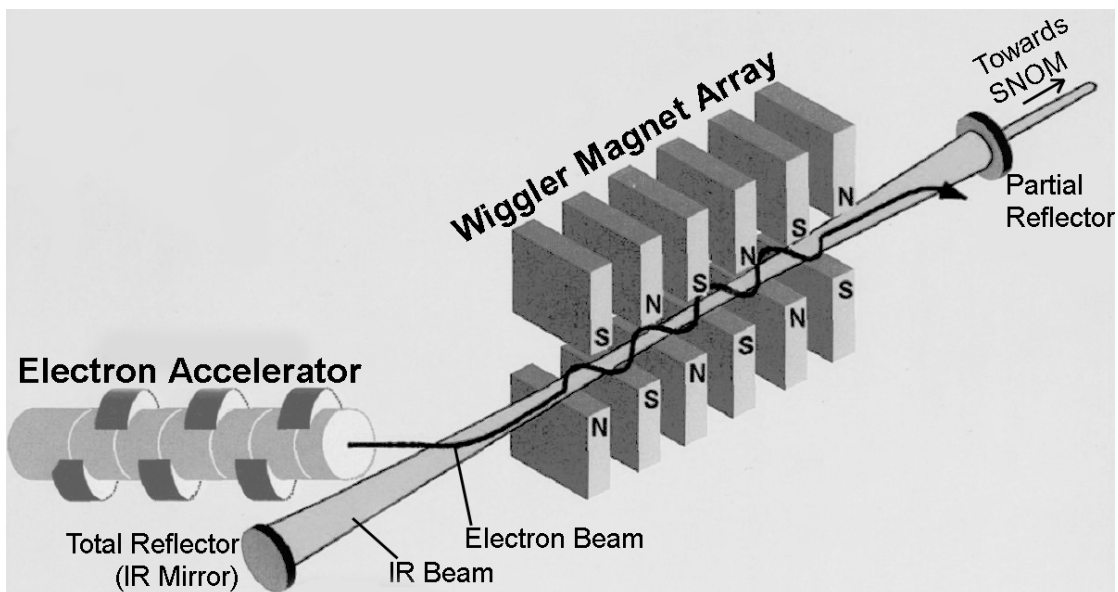


Figure 2-5: Simplified scheme of a free electron laser (FEL).

A free electron laser (FEL) was first conceived by John Madey in his Stanford PhD dissertation in 1970. The Vanderbilt University FEL, a mid-IR source used for medical and materials science research, became operational in 1992 [13]. A free electron laser consists of an electron beam source/accelerator, a periodic transverse magnetic field (a wiggler magnet), and an optical resonator (composed of one total reflection and one partial-reflection mirror). The wiggler magnets impose a transverse acceleration on the electrons (the zigzag movement of the electron beam is shown in figure 2-5), resulting in the generation and amplification of light, which co-propagates with the electron beam through the wiggler. As in a conventional laser, the resonator mirrors provide feedback around amplifying medium and build up the stored radiation. The wavelength of the laser output can be tuned by adjusting the electron energy and/or the wiggler magnetic field strength (for example, by changing the distance between the upper and the lower magnet array in the wiggler). [14]

The Vanderbilt University Free Electron Laser (VU FEL) is continuously tunable over a broad wavelength range (2.1 – 9.8 μm), and it is intense (average power of up to 11 W) and stable [13] - therefore ideal for spectroscopic IR-SNOM applications.

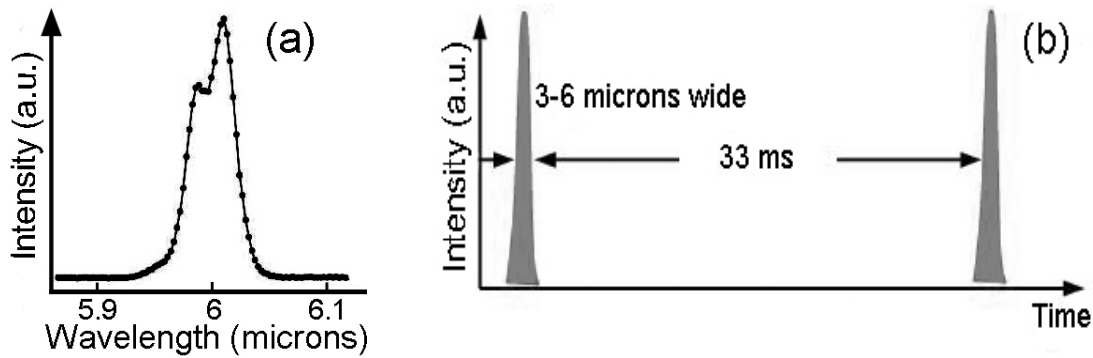


Figure 2-6: FEL pulse structure. (a) The FEL IR is not perfectly monochromatic. Its spectral width is about 1% FWHM. When the FEL is tuned to 6 μm wavelength, the emitted IR actually consists of a narrow distribution of wavelengths centered at 6 μm . (b) The FEL IR beam is composed of pulses. The pulse frequency is 30 Hz and its temporal width is 3-6 microseconds.

The VU FEL IR beam is pulsed at 30 Hz, and the IR pulse width is 3-6 microseconds, depending on the wavelength and the "tune" (figure 2-6 b). The spectral width is about 1% FWHM (full width at half maximum): when the FEL is tuned to 6 μm wavelength, the pulses are actually composed of a narrow distribution of wavelengths centered at 6 μm (figure 2-6 a). The pulse energy stability of the FEL is fairly good, but not as good as the best lasers. This was taken into account in the experiments by normalizing all the results to a picked off reference. Typical energy per macro-pulse stability is about 10% FWHM. Four dielectric coated mirrors are used to cover the entire wavelength range. Their nominal ranges are: 6 - 9 μm , 4 - 6 μm , 2.8 - 4.2 μm and 2 - 3 μm .

2.3.3 Experimental Scheme

Figure 2-7 shows the experimental scheme used in the IR-SNOM experiments. Our experiments are performed in the external reflection collection mode. In this mode, an FEL IR beam is aimed at the sample from the far-field using mirrors. The FEL beam homogeneously illuminates the sample over a broad area (~ 1 mm spot diameter). The maximal scan size of the SNOM instrument is 30×30 μm – very

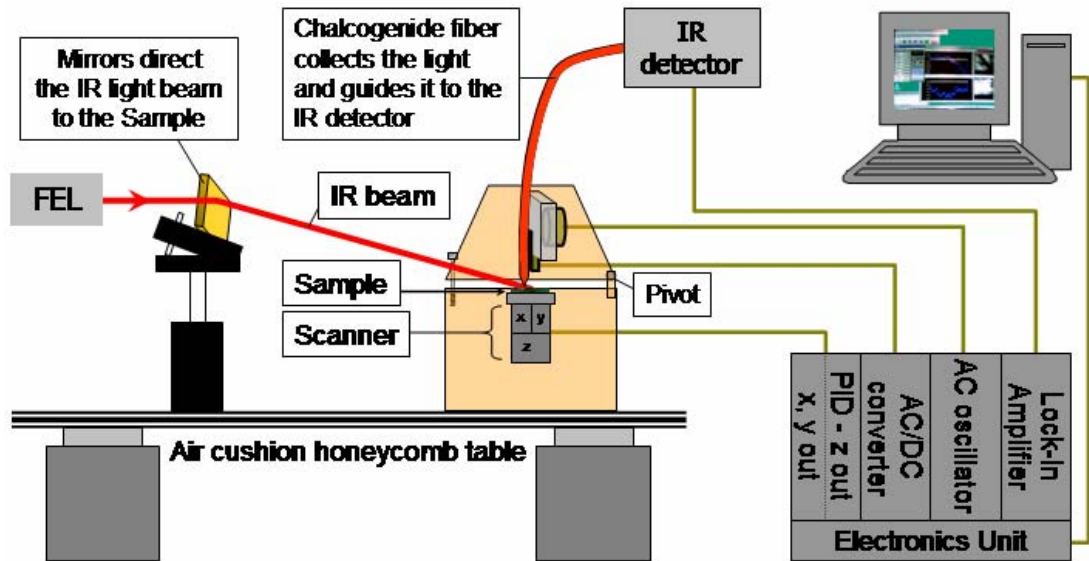


Figure 2-7: General experimental IR-SNOM scheme.

small when compared with the illuminated area. The maximal z motion of the scanner is $8\ \mu\text{m}$.

The distance between the SNOM fiber's aperture and the sample is a few nanometers during scanning, and the near-field signal varies exponentially as a function of this distance. Therefore, very small mechanical or acoustical perturbations can induce significant noise in the detected signal. To insulate the SNOM instrument from such perturbations the setup is fixed on an air cushion honeycomb table.

2.3.4 SNOM Instrument

Figure 2-8 shows a cross-section of the SNOM instrument made in the ISM-CNR laboratory in Rome, Italy, by our collaborators A. Cricenti et al. [15]. The case of the microscope consists of two cylindrical stainless steel pieces (100 mm diameter). The lower piece is attached to the table and contains the x - y and z piezo scanners. The SNOM fiber probe is fixed to the upper piece. The two pieces are connected on one side with a pivot (see figure 2-7). The microscope can be opened to place samples or

to replace a fiber by rotating the upper part upwards around the pivot. The approach screw (figure 2-8), which is across from the pivot on the other side of the cylinder, regulates the distance between the fiber and the sample (when screwed in, the fiber is approached to the sample, and vice versa). The sample is placed on the sample holder, on the top of the scanner, and scanned under the fiber aperture. The system can accommodate samples several centimeters large and several millimeters thick. The approach-screw/pivot system ensures rigidity and compactness of the system, both of which are important for SNOM instruments as they lower mechanical vibration noise levels.

The scanner consists of a piezo-electric tube [16]. Piezoelectric tubes are common scanners for the AFM, STM and SNOM. The x - y tube is divided into four parts (in figure 2-8, they are called $x+$, $x-$, $y+$ and $y-$). When a voltage $-V$, for example, is applied to the $x-$ part of the tube, and $+V$ to the $x+$ part, the $x-$ part gets shorter and the $x+$ part gets longer: the tube bends and moves the sample under the fiber tip along the x axis (in the $x-$ direction in this case). A V value of a few volts corresponds to a movement of a few nanometers.

The tapered chalcogenide fiber is glued to the bimorph piezo using phenyl-salicylate. Phenyl-salicylate is a solid crystal at room temperature, but has a melting point at only 41.5°C . A soldering iron held at a distance of a few millimeters is sufficient to liquefy it. It typically cools down and solidifies again in a few minutes. This allows an easy and quick fastening and replacement of fibers.

Since the maximal x - y piezo scanner range is $30 \times 30 \mu\text{m}$, there are also two motors that can move samples $\pm 4 \text{ mm}$ in the x - y plane (“ x motor” and “ y motor” in the figure 2-7). The motors have a minimal step of less than $1 \mu\text{m}$. For smaller movements of the sample, the piezo scanner can be used (users are free to fix the start point of the scan within the $30 \mu\text{m}$ range).

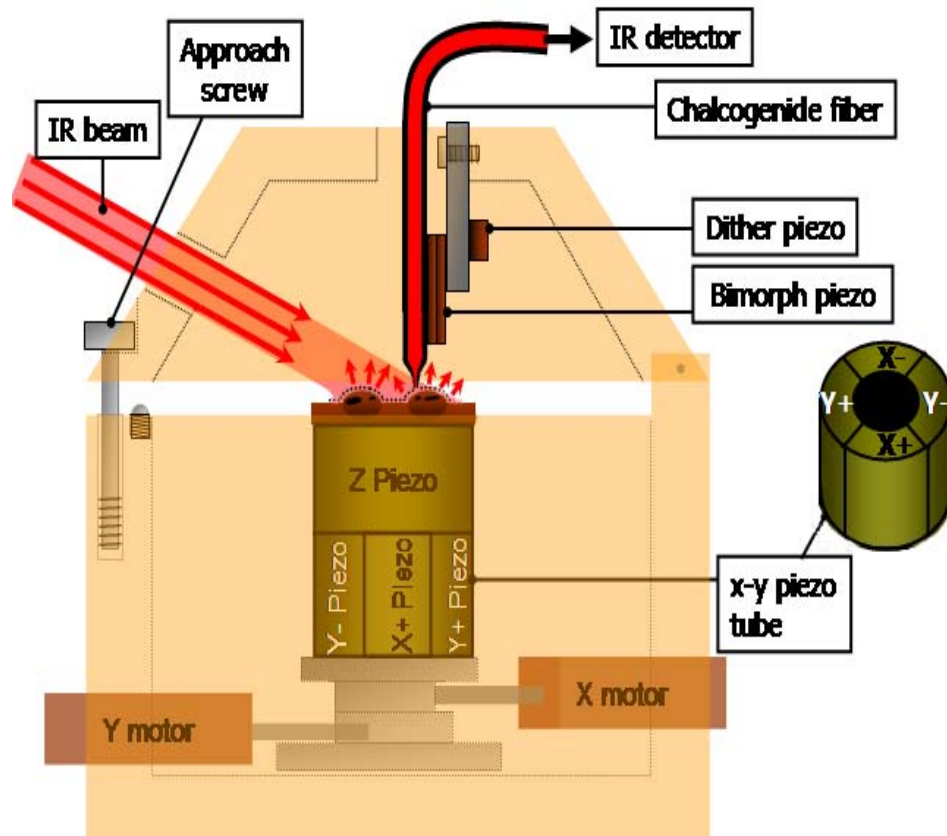


Figure 2-8: IR-SNOM module. Sample is placed on the piezo-ceramic tube scanner and illuminated from the far-field by an IR beam. It is scanned under the aperture at the tip of the chalcogenide fiber that collects near-field light and guides it to an IR detector.

2.3.5 Electronics

The lower right corner of figure 2-7 shows the “electronics” unit. This unit is divided into four subunits:

- (1) “PID - z out / x, y out” contains voltage generators that can apply voltages ranging from -200 V to +200 V to the x and y piezos, and from -500 V to +500 V to the z piezo.
- (2) “AC oscillator” is an AC voltage source connected to the Dither piezo. An AC voltage is applied at a frequency that excites a resonant vibration of the probe

(around 5 KHz for this setup), which induces a lateral (x - y plane) oscillation of the fiber. The amplitude of the oscillation is usually less than 10 nm, a value we can fix by adjusting the amplitude of the AC voltage. When the fiber's tip is a few nanometers from the sample, the amplitude of the oscillation starts to be damped by shear forces. Oscillation and bending of the fiber bends the "bimorph" piezo. The bending induces an AC voltage in the bimorph, the amplitude of which is equivalent to the tip oscillation amplitude.

(3) "AC/DC converter" converts this amplitude into an equivalent DC voltage. This voltage is fed into a feedback loop where a PID (proportional integral derivative controller) compares it with the selected reference DC value. The PID is a standard feedback loop component used in control applications. It measures the "output" of a process (the bimorph DC voltage) and controls the "input" (the value of the voltage applied to the z piezo), with the purpose of maintaining the output at a target value (the reference DC). If the bimorph DC voltage is smaller than the reference DC voltage, the feedback loop decreases the voltage that is applied to the z piezo, and vice versa. In this way the tip moves in the z direction (towards and from the sample), always maintaining the damped amplitude of the oscillation constant during scanning (typically around 90 % of the initial free oscillation un-damped amplitude value; the value chosen for the reference DC voltage determines the damping value). The sample is scanned laterally by the x - y piezos, and the z piezo simultaneously moves it up and down following the shape of the sample. SNOM produces two images: the topography is acquired simultaneously with the optical image as the values of the voltage applied to the z piezo are recorded. For a detailed description of the (1), (2), and (3) parts of the electronics unit see [17].

(4) "Lock-in amplifier" filters the signal that arrives from the IR detector and removes eventual optical noise. For the IR-SNOM experiments we filtered the signal with a gated box-car averager [18] instead of a lock-in amplifier. Gated boxcar averagers are designed to recover fast, repetitive, analog signals. The gate opening and its width (2 ns to 15 μ s) are precisely adjusted to coincide with the FEL pulses. A gated integrator amplifies and integrates the signal that is present during the time

the gate is open, while ignoring the noise and interference that may be present at other times. The boxcar averages its output over a chosen number of pulses (in our experiments, usually 10 or 30 pulses). Since any signal present during the opening of the gate will add up linearly, and the noise will add up in a "random walk" fashion as the square root of the number of shots, the averaging N shots will improve the signal-to-noise ratio by a factor of \sqrt{N} .

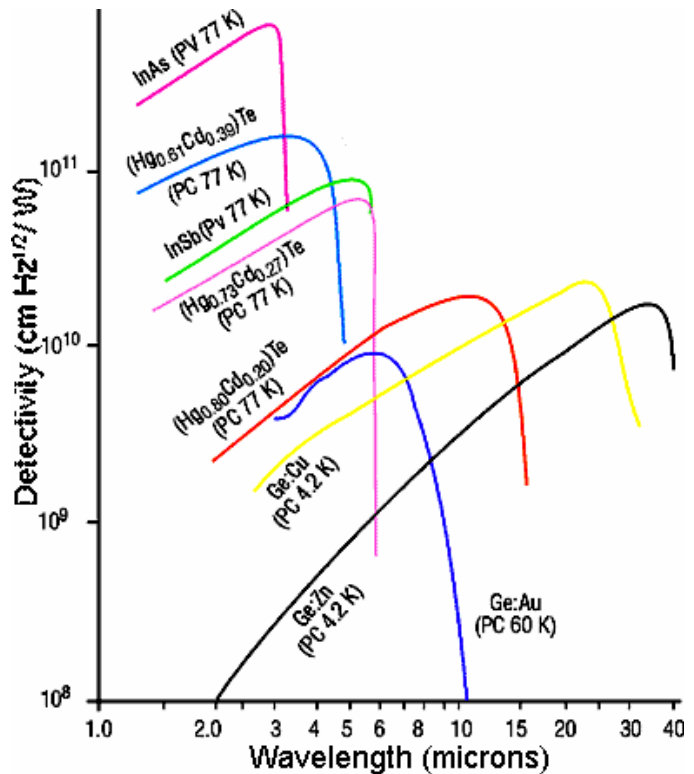


Figure 2-9: Detectivity as a function of wavelength for a number of different photodetectors operating in the infrared. The temperature of operation is indicated. Photovoltaic detectors are denoted PV; photoconductive detectors are denoted PC [20].

2.3.6 IR Detector

Figure 2-10 shows the detectivity* as a function of wavelength for the common IR detectors. We used a mercury cadmium telluride (HgCdTe) detector [19]. Its detectivity as a function of the wavelength is represented by the red line in figure 2-10. We chose this detector for its high performance over the whole FEL wavelength range. Its operating wavelength ranges from 2 to 15 μm . It is a photoconductive detector. The detector is cooled and operates at the liquid nitrogen temperature in order to reduce the internal noise. It has a 2 square millimeters active area, its typical responsivity is superior to 100 V/W, and its time constant is 0.3 μs .

* The detectivity gives a measure of the intrinsic quality of the detector material. It is defined as the square root of the detector area per unit value of the optical power that produces a signal voltage (or current) equal to the noise voltage (or current) of the detector.

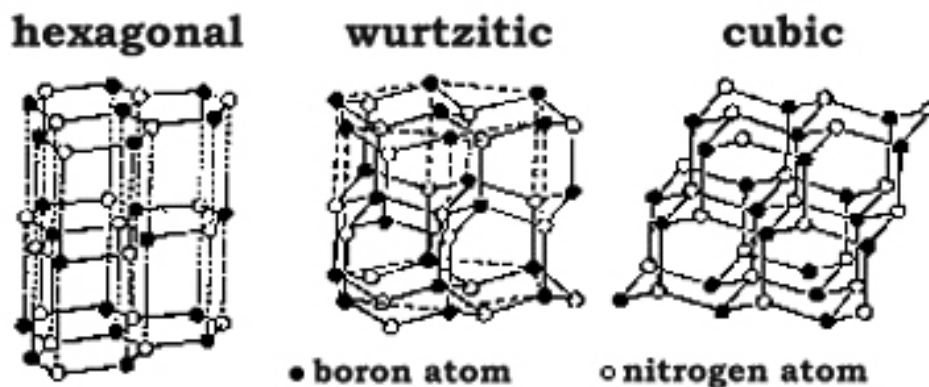


Figure 2-10: Common boron nitride crystal structures.

2.4 IR-SNOM Imaging of Boron Nitride Films

2.4.1 Boron Nitride (BN)

Boron nitride is a binary chemical compound, consisting of equal proportions of boron and nitrogen. Boron and nitrogen are neighbors of carbon in the periodic table: in combination boron and nitrogen have the same number of outer shell electrons as carbon, and their atomic radii are similar to that of carbon. It is not surprising, therefore, that boron nitride and carbon exhibit similarity in their crystal structure and properties. In the same way that carbon exists as graphite and diamond, boron nitride can be synthesized in hexagonal and cubic forms.

Cubic boron nitride (c-BN) has the same crystal structure as diamond. Its properties mirror those of diamond: extreme hardness (c-BN is the second hardest material after diamond), excellent chemical inertness, thermal stability and a wide band gap characterize c-BN. Unlike diamond, BN does not occur in nature and it has to be synthesized in a laboratory. Cubic boron nitride is superior to diamond in certain aspects. When diamond is heated up by friction in the presence of air, it tends to

decompose into carbon dioxide while c-BN stays inert. Cubic-BN also does not dissolve into iron, nickel and related alloys at high temperatures, while diamond does.

These properties recently stimulated an important amount of research on c-BN film synthesis. The growth of c-BN is difficult: the typical crystal phase of BN

films is a mixture of cubic, wurtzitic and hexagonal crystals [21]. Hexagonal boron nitride (h-BN) is the equivalent of graphite, both in structure and in properties, and is undesired when synthesizing c-BN. The wurtzite BN (w-BN) properties (hardness, chemical inertness) are more similar to those of c-BN. Figure 2-10 shows the three common BN crystal structures.

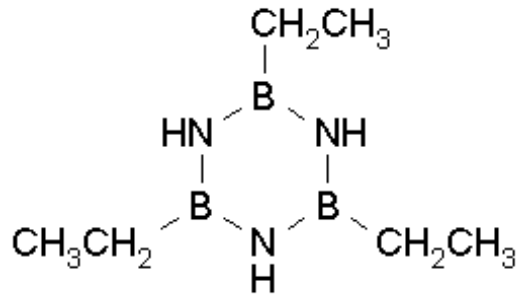


Figure 2-11: Triethylborazine structure. Triethylborazine is used as a precursor in the LCVD synthesis of BN.

2.4.2 Laser Chemical Vapor Deposition (LCVD) of BN Films

Our collaborators (B. Ivanov et al.) at Vanderbilt University have grown BN films by laser chemical vapor deposition (LCVD). In a LCVD process the substrate is exposed to one or more volatile precursors, which react and/or decompose on the substrate surface to produce the desired deposit.

Mono-crystalline (100) Si is used as a substrate. It is held at room temperature during the deposition. The 2, 4, 6 - triethylborazine (TEB) is used as a BN precursor (figure 2-11) [22]. The precursor container is heated up to reach a vapor pressure of the order of 0.5-1 Torr. Laser energy was supplied by the FEL beam with a 40 mJ pulse energy and 30 Hz repetition rate. The FEL beam is focused on a 250 μm spot on the surface of the Si substrate using a 100 mm focal length BaF₂ lens. The spot can be scanned during the deposition with the scan speed of 20 to 70 $\mu\text{m/s}$. The FEL is

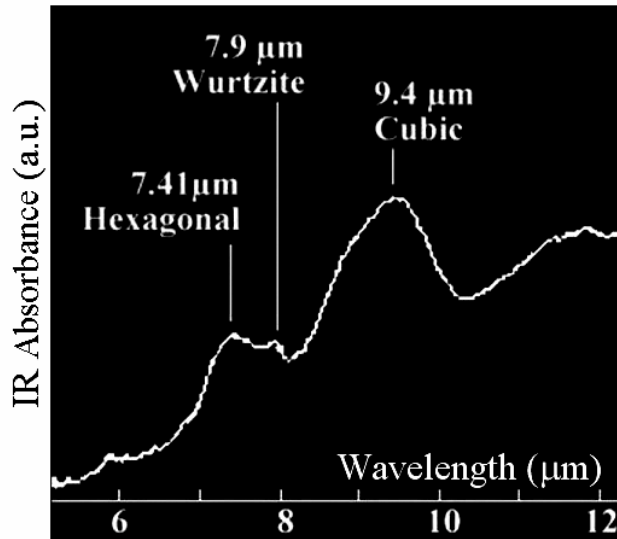


Figure 2-12: FTIR spectrum of the BN films shows absorption peaks typical of cubic, wurtzite and hexagonal crystal structures of BN.

tuned to deliver the 3.43 μm wavelength IR beam, which corresponds to the ethyl vibrational mode absorption of the TEB precursor. Irradiation at this wavelength increases the probability of breaking the bond between the ethyl radical and the B_3N_3 ring.

The deposition occurs on the substrate at the point where the laser is focused. The scanning enables a controlled laser-

assisted writing of around 200 μm wide BN stripes.

2.4.3 BN Results

The boron nitride films were first examined with the Fourier transform infrared spectroscopy (FTIR). Various phases of BN were identified by their well-known IR absorptions (figure 2-12). The features at 9.4, 7.9 and 7.4 μm are associated respectively to the cubic, wurtzite and hexagonal BN crystal phases [23, 24]. This showed that the three BN crystals coexist in the films.

The IR-SNOM experiment targets the vibration modes that correspond to these crystallographic BN phases. At each scan site we performed three SNOM scans with the FEL illumination that was tuned to a different wavelength every time: the 9.4 μm wavelength IR absorption reveals the presence of c-BN, the 7.9 μm wavelength IR absorption reveals the presence of w-BN, and the 7.4 μm wavelength IR absorption reveals the presence of h-BN.

Figure 2-13 shows the corresponding IR-SNOM images. As explained previously, each scan allows the simultaneous acquisition of two images: the topographic image (2-13a, c and e) and the optical image (in this case, reflected IR intensity) (2-13b, d and f). The 2-13a topography corresponds to the 2-13b optical image; 2-13c is acquired at the same time as 2-13d, and 2-13e is acquired at the same time as 2-13f. Figure 2-14a shows the cross-sections of the topography that corresponds to the line A-B in 2-13c, while figure 2-14b shows the cross-section of the reflection intensity that corresponds to the line C-D in 2-13d.

Before starting a scan, the FEL illumination spot is moved across the surface of the sample and positioned so that its center is under the SNOM aperture. This is achieved by adjusting the inclination of the mirror that directs the IR beam onto the sample until we obtain the maximum reflection intensity collected by the SNOM aperture. We tested different beam-sample incident angles (in the z plane), and conducted most of our experiments with the angle in the 10° to 20° range. This angle ensures reflection from the BN samples. The SNOM images are typically acquired over a $20 \times 20 \mu\text{m}$ sample area, with a minimum of 200 acquisition points per scan line (in which case a total of 200×200 acquisition points, and the same number of pixels, constitute the final SNOM images). The time to complete this kind of scan is approximately 40 minutes[†]. The pulse energy of the FEL IR beam is adjusted to around $300 \mu\text{J}$, the value that typically ensures an IR-SNOM signal more than 10 times superior to the noise level before the boxcar averaging.

The topographic images in figure 2-13 (a, c and e) show that the three scans were performed over the same sample zone. This indicates that the SNOM apparatus maintains a good stability over a period of more than two hours (stability can be problematic with some commercial SNOM instruments). The darker color indicates more absorption in the optical images.

[†] The scan time can be decreased by increasing the PID gain, but that often results in an increased noise levels.

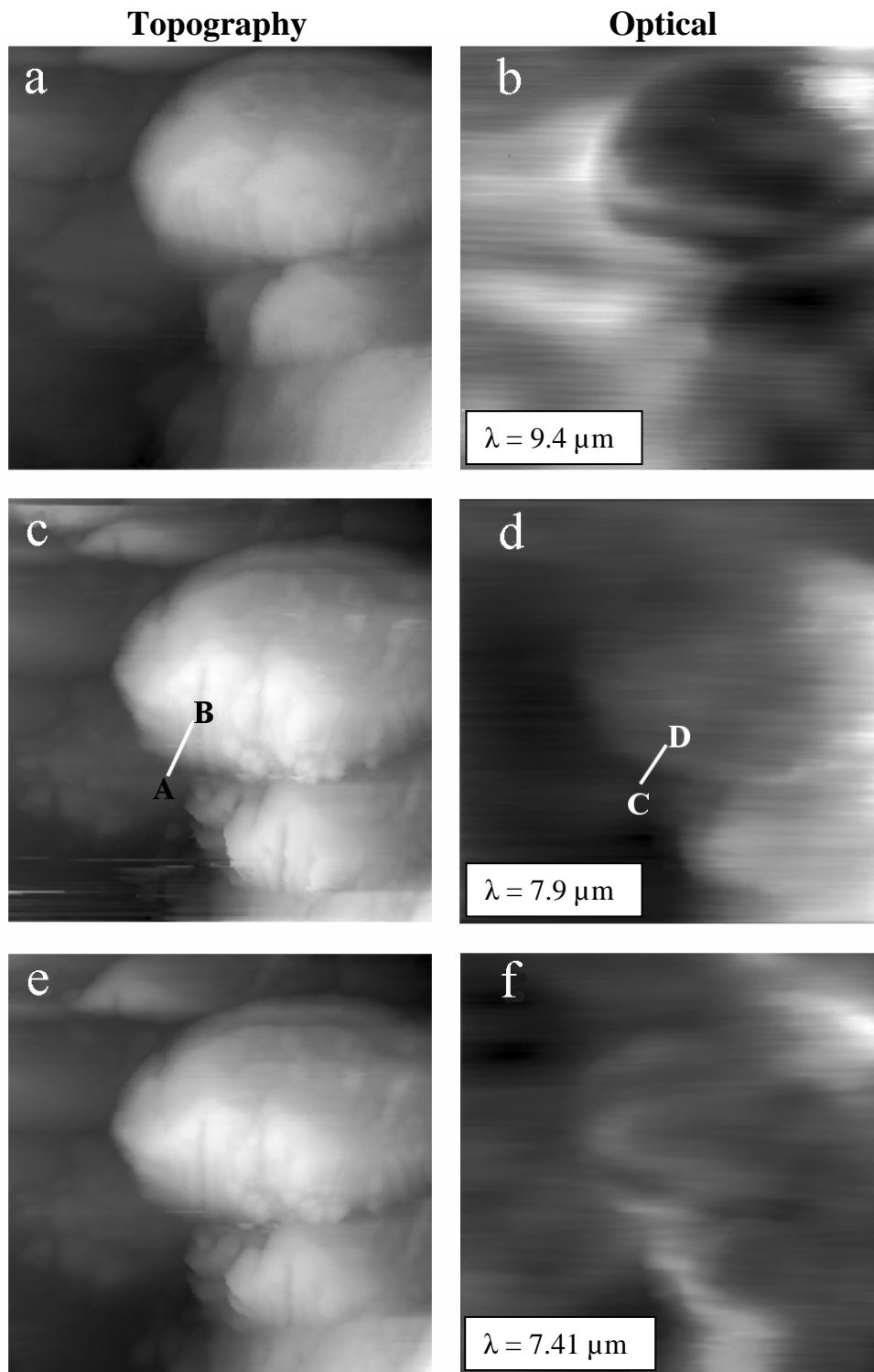


Figure 2-13: IR-SNOM imaging of a BN film. With each $20 \times 20 \mu\text{m}$ scan two images are simultaneously acquired: a topographic image and an optical image; 2-13a and b show respectively the topography and the reflection intensity acquired with the FEL illumination tuned to $9.4 \mu\text{m}$ wavelength; 2-13c and d were recorded with the illumination wavelength at $7.9 \mu\text{m}$; 2-13e and f with $7.41 \mu\text{m}$. Absorption at $9.4 \mu\text{m}$ reveals the position of the cubic BN crystals; at $7.9 \mu\text{m}$, the position of the wurtzite BN, and at $7.41 \mu\text{m}$ the position of the hexagonal BN crystalline form.

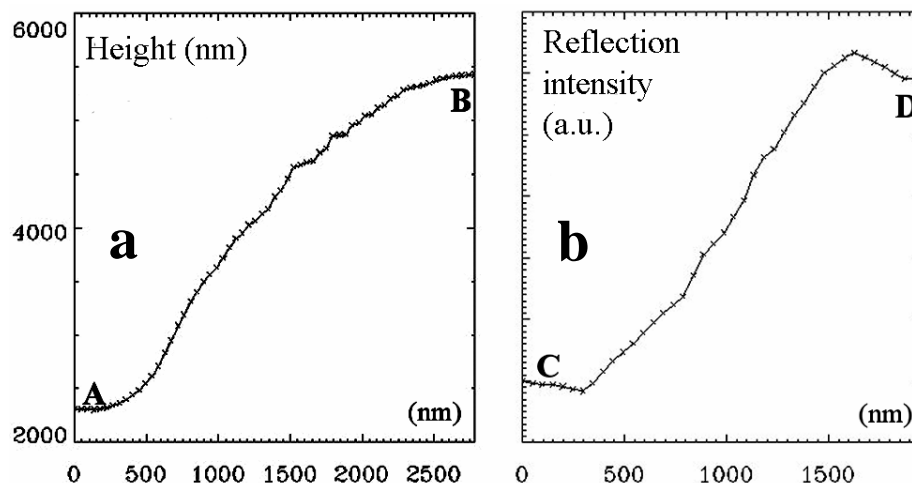


Figure 2-14: Cross-sections of the topography and of the reflection intensity shown in 2-13; 2-14a is a topography cross-section corresponding to the line A-B in figure 2-13c; 2-14b is an intensity profile corresponding to the line C-D in 2-13d.

The topography reveals a very granular structure of the BN. The cross-sections, such as the one shown in figure 2-14a, show that the grains are typically 2 to 4 μm high; the topography images, such as 2-13a, show that the grains are 10 to 15 μm wide.

The optical images clearly reveal differences in the lateral distribution of different BN crystal forms. The strongest absorption from the c-BN (figure 2-13b) arises from the three large grains that can be seen on the right side of the topographic images (figure 2-13a). On the contrary, the wurtzite phase (figure 2-13d) is mainly present in the flat parts of the sample, closer to the substrate. A weak hexagonal contribution (figure 2-13 f) seems to come from all over the sample. The lower h-BN absorption intensity can be explained by the possibility that the h-BN is on the interface with the substrate, under the layer of the w-BN and c-BN. This possibility is confirmed by similar observations reported in [26], where BN films were etched and the film composition was examined at different etching depths by FTIR. The results of that study show that a thin layer of h-BN exists at the interface between a c-BN layer and the Si (100) substrate.

SNOM offers several advantages over the experimental technique used in [26]. First, it is a non-destructive technique. Second, it takes into account eventual variations of

composition in different parts of the sample (which are completely neglected by the techniques used in [26]). Third, SNOM provides additional information, such as the eventual granularity of the sample (also completely ignored in [26]). Thus, the IR-SNOM approach offers a much larger insight into the sample properties and a better understanding of what really occurs during the deposition.

Figure 2-14b shows a cross-section of the reflected signal that corresponds to the line C-D in figure 2-13d. This cross-section indicates a resolution of approximately $1\ \mu\text{m}$, while the illumination wavelength was $\lambda = 7.94\ \mu\text{m}$. Thus, we achieved a resolution of around $\lambda/8$, which is at least 4 times better than the one imposed by the diffraction limit. We believe that the actual resolution of our setup is much higher, as the following results will demonstrate. The BN films are very thin when compared with the illumination IR wavelengths. Even when reflected, there is a significant penetration of the evanescent illumination field into the sample. The depth of penetration of the evanescent field is greater with longer wavelengths (equation 1.12 in Chapter 1, section 1.4.4). Thus, the illuminating IR field penetrates into the sample and, due to its long wavelength, is absorbed by the parts of the sample that are several microns beneath the surface. If the sample is constituted of relatively fine layers, this can significantly lower the apparent resolution.

We have performed over a hundred similar IR-SNOM scans on different scan sites and on three different BN films. Over 80 % of the results reveal the same BN structure like the one shown in figure 2-13. Preliminary BN results have been published [27], and a more detailed study has recently been accepted for publication [28].

Comparisons between IR-SNOM topographic and spectroscopic images enabled a quick and clear characterization and understanding of the BN structure. Even a combination of several other research techniques could hardly give such an accurate image of this kind of sample.

2.5 IR-SNOM Study of Lithium Fluoride Color Centers

Figure 2-15 shows the results of IR-SNOM tests that were performed with lithium fluoride (LiF) films deposited on silicon substrates. In this case, the aim was not to study the lateral distribution of different chemical species but the lateral changes in the refractive index induced by x-ray bombardment.

2.5.1 Lithium Fluoride (LiF) Color Centers

Many kinds of ionizing radiation induce the formation of stable, visible emitting electronic defects in LiF crystals and thin films. The defects are called “color centers” because of their influence on the color of the crystal [29]. The color centers could be exploited for the fabrication of miniaturized optical devices. The creation of the color centers would be a critical step in this fabrication procedure [30-33]. Explored in this study are the results of an innovative irradiation technique based on extreme ultraviolet (EUV) radiation and soft X-rays emitted by a plasma-point source [33]. This approach is very interesting because it can produce patterned coloration over large areas (measuring several square centimeters).

2.5.2 Colored LiF Pattern Preparation

High-quality LiF films were grown by thermal evaporation on untreated silicon substrate [34] kept at 250°C during the deposition. The films’ thickness, measured by a stylus profilometer after the growth, was around 800 nm.

The EUV and soft X-rays are obtained by focusing a powerful excimer laser beam on a solid target placed in a vacuum chamber. The point on which the laser is focused becomes a plasma source and generates a plasma plume. The excimer laser used here

is a non-commercial, large-volume laser developed at the ENEA Laboratories in Frascati, Italy. It operates at the emission wavelength of 308 nm. Using a 10 ns pulse, the laser intensity on the target is 3×10^{13} W/cm². The X-ray emission of the plasma point source covers the spectral interval of 0.8-60 nm (1.5 keV-20 eV). This corresponds to the entire EUV region and to a part of the soft X-ray region [35]. The LiF sample is placed in the same vacuum chamber, around 12 cm from the plasma source. This irradiation method enables the exposure of a large LiF area of several square centimeters in a single shot of the excimer laser. A regular colored pattern is obtained by placing a copper mesh (wire diameter 10 μm, period 12.7 μm) on the LiF films.

2.5.3 LiF Results

Figure 2-15a shows a fluorescence optical micrograph of the colored pattern. The white spots correspond to the areas irradiated by X-rays.

Figure 2-15b is a 24×24 μm² shear force (SNOM topography) image showing the LiF surface (see the corresponding profile in figure 2-15c). It is a rather smooth surface, with well resolved small features that do not exceed several hundred nanometers in height. Figure 2-15d shows the corresponding optical (reflectivity) SNOM image taken with the FEL illumination beam wavelength of 6.1 μm. At this wavelength we can clearly observe contrast in the image that is not correlated to the topographic SNOM features, and which shows a periodicity that corresponds to the pattern shown in figure 2-15a. Similar results were obtained with images taken at a wavelength of 9.2 μm. Since there is no particular LiF absorption in this spectral region, we ascribe the change in reflectivity to the irradiation-induced variation of the refractive index of the exposed LiF material. A modification of the complex refractive index of LiF by the stable formation of color centers embedded in it was recently studied [36]; it was shown that the modification is related to the density of the color centers [37], which is proportional to the X-ray exposure dose.

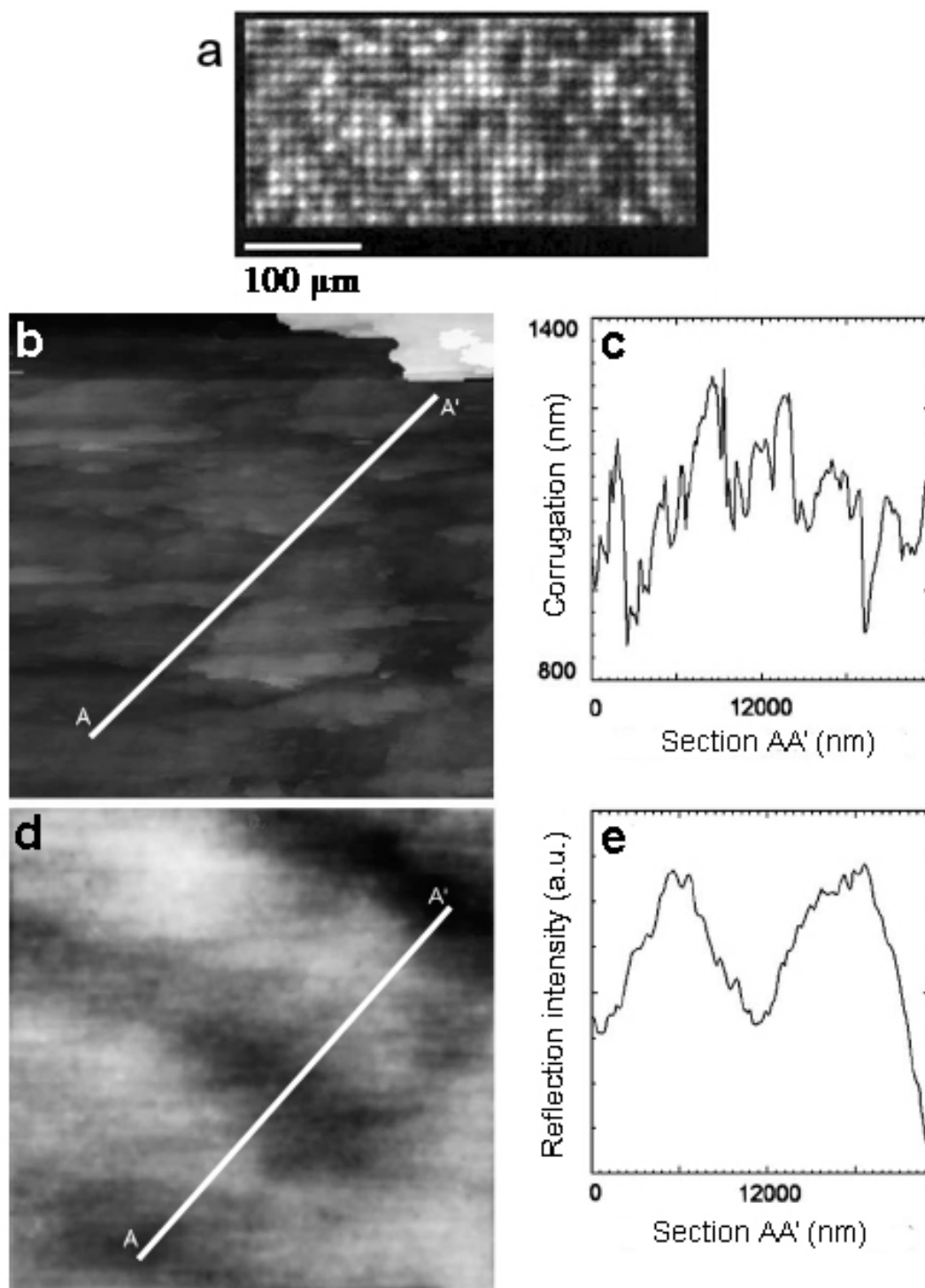


Figure 2-15: IR-SNOM images of a LiF film on silicon with patterned coloring by x-ray irradiation (see [21]). (a) Fluorescence optical micrograph of the colored pattern (the white spots correspond to irradiated areas). (b) $24 \mu\text{m} \times 24 \mu\text{m}$ SNOM shear force image. (c) Intensity profile that corresponds to the AA' line of figure 2-15b. (d) Spectroscopic (reflectivity) SNOM image taken with a wavelength of $6.1 \mu\text{m}$. (e) Intensity profile that corresponds to the AA' line of figure 2-15d.

Figure 2-15e shows an intensity profile that corresponds to the line A-A' in figure 2-15d. From such profiles we estimated a lateral resolution of 200-300 nm (50 nm in the topographic images), which again is much better than the diffraction limit that corresponds to the 6.1 and 9.2 μm wavelengths. This work has been published in [38].

2.6 IR-SNOM Cell Imaging

2.6.1 Motivations

The importance of IR spectromicroscopy in bio-medical research is growing rapidly. Various molecular components of cells produce a characteristic IR spectrum that is rich in structural and functional details [39, 40]. The most exciting applications of the IR-based techniques concern cancer research. IR spectroscopy can detect and monitor characteristic changes in molecular composition and structure that differentiate normal from cancerous cells [41-45]. IR analysis is even more interesting since it causes no damage to the cells. Recently, IR microscopic techniques have been used in diagnosing various types of cancer in human tissues and in characterizing different kinds of cells [46-48]. The principal limitation of this field of research is the lack of spatial resolution that arises from the diffraction limit. Efforts have been made to increase the resolution, for example by using synchrotron radiation (as an ultra-bright IR source) in combination with a doubly confocal microscope [49, 50]. The resulting resolutions have been between 5 and 10 μm . This is insufficient for IR spectromicroscopy studies of inner cellular structures.

After successful tests with material science samples, we decided to test the possibilities of the IR-SNOM with samples most commonly studied with conventional microscopes: cells.

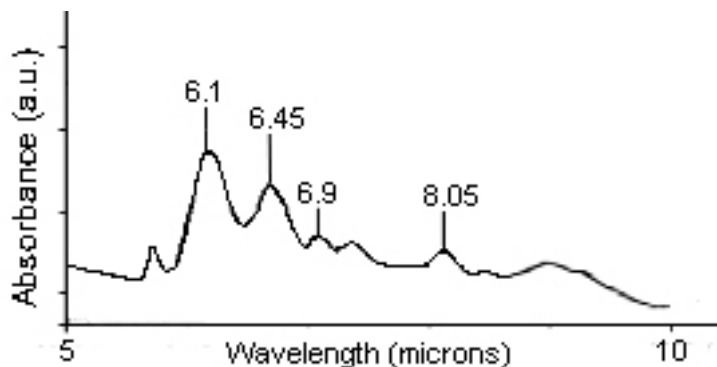


Figure 2-16: Typical cell IR spectrum between 5 and 10 μm . Absorption peaks at 6.1 μm and 6.45 μm are amide I and amide II protein bands. Absorption at 6.9 μm is the lipid CH_2 deformation band, and the absorption at 8.05 μm is the asymmetric PO_2^- DNA absorption band.

2.6.2 Targeting Specific Cell Constituents

Cells were seeded on glass cover-slides, placed in the SNOM instrument and illuminated with the VU FEL IR beam, which was tuned to specific wavelengths. The local reflected IR was picked up from the surface of the cells by the SNOM aperture.

The VU FEL was tuned to the IR wavelengths that are absorbed by several chemical bonds that are present in specific cell constituents. The SNOM images presented in figure 2-18 were acquired with three illumination wavelengths: 6.1 μm , 6.95 μm and 8.05 μm .

All cells exhibit strong IR absorption peaks at these three wavelengths (figure 2-16). The cell constituents that absorb the wavelengths are proteins, lipids and nucleic acids.

The 6.1 μm wavelength radiation is absorbed (figure 2-17) by the protein amide $\text{C}=\text{O}$ bond, where it induces the stretching vibration excitation [51]. This absorption band is commonly called the amide I band. The localization of the absorption at this wavelength reveals the position of proteins, and the absorption intensity reveals the

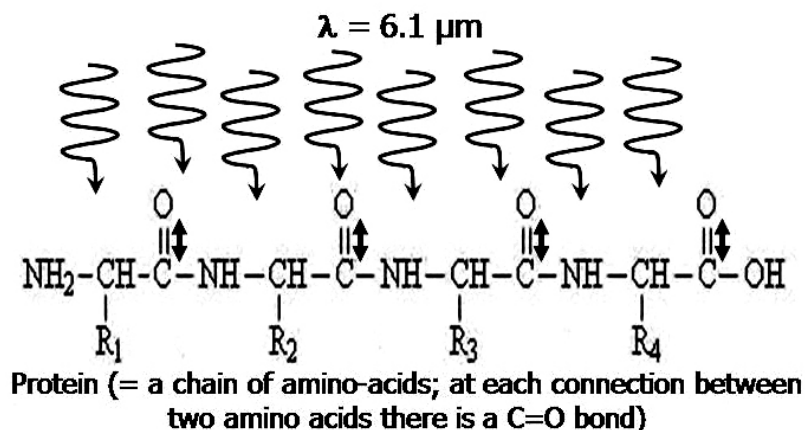


Figure 2-17: When the IR radiation with a wavelength of $\lambda = 6.1 \mu\text{m}$ illuminates proteins, it is strongly absorbed, which excites the C=O bonds stretching vibrations. Constituents of cells other than proteins do not absorb the IR radiation at this wavelength.

protein density. This absorption band is also sensitive to the secondary structure of proteins [52, 53]. The amide I absorption band has been extensively studied by organic IR spectroscopists and shown to have the strongest absorption in the IR spectrum of cells.

The IR absorption centered around $6.95 \mu\text{m}$ corresponds to a methylene group vibration in fatty acids. This absorption is one of the well-known methyl and methylene bands that is highly characteristic for lipids in the membranes and other lipid structures [54, 55]. We are conducting a new series of experiments targeting lipids with the IR light tuned also to $3.41 \mu\text{m}$ [50].

The absorption at $8.05 \mu\text{m}$ originates from the asymmetric stretching mode of phosphodiester groups (PO_2^-) in nucleic acids [50]. Thus, this IR absorption is expected to occur only in the nucleus.

These three IR wavelengths were not chosen only for the purpose of studying the distribution of proteins, lipids and DNA within cells. The ratios of the IR absorption intensity of these species have been found to be different in normal and cancerous cells [42, 45], and to change as the cells undergo necrotic, apoptotic and division processes [50]. It was shown [48] that the infrared spectra, and more particularly the

lipid/protein band ratio, reflect in vitro migration properties of cancerous cells (i.e. motility and invasiveness), as well as their in vivo aggressiveness.

2.6.3 Cell Preparation

We performed IR-SNOM imaging experiments with several cell types, such as green monkey kidney fibroblast cells (COS cell line), human keratinocyte cells (HaCaT cell line), and rat pancreatic cells (beta cell line INS-1) [38]. Figure 2-18 shows SNOM images of human keratinocyte cells (HaCaT cell line). The cells were seeded on glass cover slides. After 24 hours the growth medium was removed and the cells were fixed in paraformaldehyde and washed twice with phosphate-buffered saline (PBS) and twice with distilled water.

2.6.4 Results

Figure 2-18 shows three images of a HaCaT cell. Figure 2-18a shows the topography of the cell. A topographic image was acquired with each of the three scans; the resulting three topographic images were identical with the one shown in 2-18a. Figures 2-18b, c and d are optical images that show the intensity of the reflected light acquired with the IR-SNOM at the wavelengths 8.05 μm , 6.95 μm and 6.1 μm . The absorption (darker color) indicates the position and density of the DNA in figure 2-18b, the lipid distribution in figure 2-18c, and the cell's protein distribution in figure 2-18d.

The comparison between 2-18d and 2-18a shows that there is a fairly homogeneous absorption throughout the cell. This signifies that proteins are homogeneously distributed in cells, which is an expected result.

Figure 2-18e shows a cross-section that corresponds to the line A-B of figure 2-18d. It demonstrates a SNOM resolution of the order of 100 nm, or $\lambda/60$. This is at least 30 times better than the resolution that is achievable with diffraction-limited lens-based microscopes.

Figure 2-18c shows an absorption intensity variation where the whole right side of the cell is darker, indicating a higher lipid density. Despite this intensity variation, when compared with the surrounding glass cover slide, the absorption can clearly be seen over the whole surface of the cell. The absorption at 6.95 μm originates from the cell membrane, which is mainly composed of lipids (a cell membrane is basically a phospholipid bilayer). Current theories of membrane structure suggest that cell membranes contain domains called lipid rafts. Lipid rafts are composed of the same constituents as the rest of the membrane: lipids, but whose fatty-acid chains are mostly straight, aligned and tightly packed into highly ordered domains. These rafts float freely within the liquid-disordered bilayer of cellular membrane and seem to play a key role in assembling protein complexes and initiating signal transduction processes [58, 59]. Since the lipid density in lipid rafts is much higher than in the rest of the membrane, the intensity of the IR lipid absorption bands should also be much higher in the rafts. Thus, the intensity variation in figure 2-18c might be the first IR observation of lipid rafts[‡], and also the first direct lipid raft imaging without the use of any kind of fluorescent dyes.

Figure 2-18b shows important absorption occurring only in a localized part of the cell (the area is encircled by a white dotted line). This strong absorption is due to the localization of the DNA inside the nucleus. FTIR measurements show only a very low absorption at this wavelength.

[‡] We will further verify this possibility by SNOM imaging of cells with IR illumination tuned to wavelengths that correspond to other lipid absorption bands.

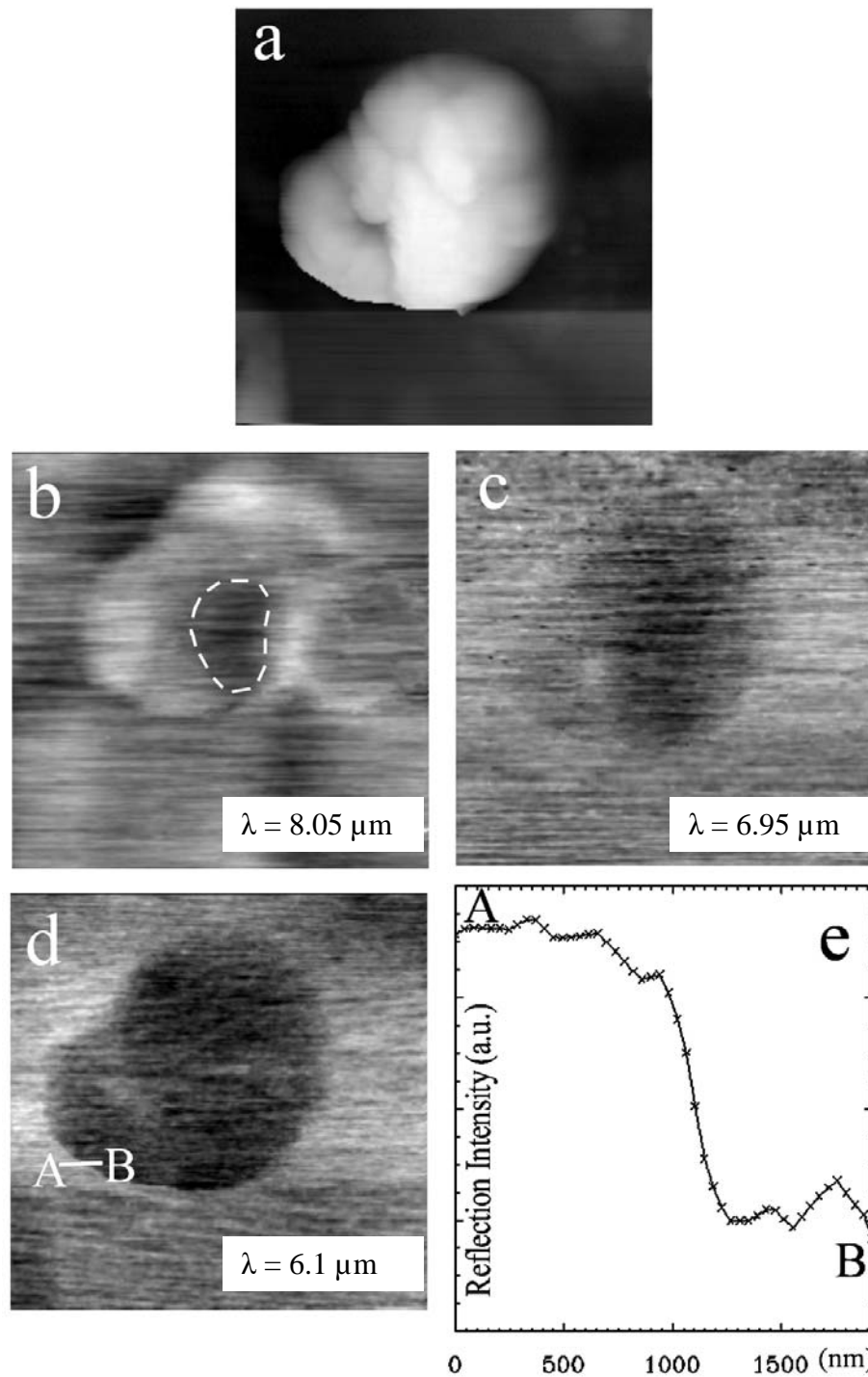


Figure 2-18: Cell SNOM images; 2-16a shows the cell topography; 2-16b, c and d are corresponding reflectivity SNOM images acquired with the illumination wavelengths $8.05 \mu\text{m}$, $6.95 \mu\text{m}$ and $6.1 \mu\text{m}$ respectively; 2-16e shows the intensity profile that corresponds to the line A-B in 2-16d; 2-16e indicates that the resolution of the IR-SNOM is around 100 nm (or $\lambda/60$, at least 30 times superior to the resolution of conventional lens-based microscopes).

Such an absorption has been seen in cells with FTIR only during replication, possibly because of the spatial extension of the nucleus [50, 60]. This is the first time ever that the inner cellular structures were resolved using an IR illumination imaging.

2.7 IR Signal Sufficiency

Signal sufficiency is an important issue concerning the aperture-based IR-SNOM. Equation 1.11 (Chapter 1, section 1.4.4) shows that the transmission coefficient of the SNOM aperture is proportional to d^4/λ^4 , where d is the diameter of the aperture and λ the light wavelength. Therefore, the IR sub-wavelength aperture transmission is even more limited than that of the visible light when using the same aperture size. Furthermore, the detectivity of the IR detectors is lower than that of the visible detectors. Figure 2-9 shows that the detectivity of the HgCdTe IR detector that was used during this thesis is approximately 10^{10} cm Hz^{1/2} W⁻¹, while the detectivity of an avalanche photo diode that works in the visible spectral domain or in the near-IR is approximately 10^{13} cm Hz^{1/2} W⁻¹ [25].

However, in practice, with the FEL IR pulse energy at 300 μ J, the HgCdTe detector output is a pulse of around 300 mV, while the noise level is less than 10 mV (and all this before the boxcar averaging and amplification).

These signal levels could be explained by the illumination light enhancement that is due to the imperfections in the fiber's gold coating. As a matter of fact, small grain-like imperfections in the gold coating near the fiber's aperture can enhance the illumination field by the lightning rod and/or surface plasmon resonance effects [61, 62]. This would cause the illumination field to be concentrated and amplified at the very tip of the fiber, under the aperture, and would greatly increase the signal-to-noise ratio.

2.8 A Review of Recent Developments in the Field of IR-SNOM

Recently, several IR-SNOM experimental setups were developed. The FEL-based IR-SNOM setups, similar to the setup presented in this thesis, were developed by two research groups: (1) a SNOM instrument operating in a photon scanning tunneling microscope configuration has been used in combination with the CLIO FEL in Paris, France [63]; (2) the Stanford FEL IR-SNOM setup [64] is almost conceptually identical to the IR-SNOM instrument that has been described in this thesis. The main difference resides in the fact that the experiments described in [64] were performed in the illumination mode (where the SNOM aperture is used as a sub-wavelength light source). A resolution of $\lambda/4$ (namely $2\ \mu\text{m}$ with the illumination wavelength $\lambda = 8\ \mu\text{m}$ [64], and $1\ \mu\text{m}$ with the illumination wavelength $\lambda = 4\ \mu\text{m}$ [63]) has been demonstrated with both the Stanford and the CLIO SNOM instruments. This is still far from the $100\ \text{nm}$ ($\lambda/60$) resolution presented in this thesis.

While the use of a free electron laser source limits IR-SNOM applications to relatively few researchers who can access such a device, the general technique can be applied with alternative tunable IR laser sources. A $450\ \text{nm}$ resolution ($\lambda/7.5$ at $3.4\ \mu\text{m}$ wavelength) has been observed in images of micro-patterned thin gold films using an aperture-based SNOM combined with a broad bandwidth IR laser that is based on an optical parametric amplifier (OPA) [65]. IR-SNOM measurements have also been performed using a color center laser pumped by a Kr^+ laser for polymer patterns imaging [66, 67].

Recently, two research groups developed apertureless IR-SNOM instruments. Contrast in vibrational absorption on a scale of about $100\ \text{nm}$ was obtained with a CO_2 laser illumination at $10.6\ \mu\text{m}$ wavelength using an apertureless SNOM [68]. An apertureless SNOM using a tunable CO_2 laser was also used for patterned DNA sample imaging with a resolution of approximately $200\ \text{nm}$ [69].

FEL being an extremely expensive light source, the future and popularization of the IR-SNOM technique depends on the development of table-top tunable IR laser sources. For the moment, such lasers have a very limited tunability (wavelengths can be tuned from 9.2 to 10.8 μm for the CO_2 lasers, and from 2.3 to 3.25 μm for the pumped color center laser [67]). The most promising table-top tunable IR sources seem to be the OPA-type lasers, similar to the one described in [65]. Their emission has been demonstrated to cover the whole mid-IR wavelength range.

From a resolution point of view, the apertureless IR-SNOM technique seems very promising, although for the moment its best resolution [68] is equal to the resolution achieved in the experiments presented in this thesis.

Most of the IR-SNOM images published until now show test measurements, performed on relatively simple samples, having a low corrugation and sharp contrast mechanisms. Among the experiments cited above, only the Stanford SNOM group [64] has tried to image cells – samples that have several microns high corrugations, are soft, and have a very complicated absorption pattern due to their extremely heterogeneous chemical composition. The resolution that they achieved [64] is quite low (around 2 μm), probably due to the fact that the experiments were conducted in the illumination mode (where the sample is illuminated through the SNOM aperture). In this mode the FEL intensity must be greatly decreased in order not to damage the fiber's metal coating, which consequently lowers the signal-to-noise ratio.

The work presented in this thesis remains unique in the sense that it is not a collection of test measurements. The samples studied in this work were not produced with the aim of testing the SNOM equipment, but as a part of broader research projects. The IR-SNOM was just one of the techniques that were used to further characterize these samples, but it proved to be capable of gathering an important amount of information that could not be obtained with other experimental techniques.

2.9 Conclusion

The experiments shown here demonstrate that the spectroscopic IR-SNOM is an extremely powerful analytical technique. It combines the IR spectroscopy's high chemical specificity with the SNOM's high optical and topographical resolutions.

Lithium fluoride and cell IR-SNOM images show a resolution of 100 nm. This resolution corresponds to a value of $\lambda/60$, which is more than 30 times better than the best possible lens-based microscope resolution.

Comparisons between IR-SNOM topographic and spectroscopic images enabled a quick and clear characterization and understanding of the BN structure. Even a combination of several other research techniques could hardly give such an accurate description of this kind of sample.

Cell imaging is probably the most exciting application of the IR-SNOM presented in this thesis. It demonstrates that the technique is fully applicable to biological samples. The resolution achieved has the same value as the resolution achieved when imaging materials science samples. The images presented are unique. Recently, several articles showed highly resolved IR spectroscopic images of cells [50, 64]. However, this high resolution never exceeded a value of several microns, which is very far from the 100 nm resolution presented in this thesis. The cell images show that it is possible to resolve inner cellular structures, such as the cell's nucleus. This is the first time that inner cellular structures have been imaged with IR illumination. The lipid raft imaging demonstrates that the IR-SNOM can tackle some of the hottest research topics today, and this, in a unique, non-invasive way, without the use of any contrast agents or dyes that are known to have an effect on the structure and behavior of the imaged constituents [70].

Presently, IR-SNOM is a mature tool, ready for applications both in materials science and in bio-medical research. Yet, further developments of the apertureless

SNOM and IR sources could soon transform it into a widely used and even more potent instrument. The development of the apertureless SNOM technique could further increase the resolution by more than an order of magnitude to achieve 10 nm-scale imaging [68]. More closely related to the IR spectroscopic capabilities is the development of table-top high-brightness IR sources that would cover the whole mid-IR spectral range. Some OPA-type light sources already have these characteristics [65]. Broad bandwidth sources are even more promising than the tunable ones, because, with sufficient brightness, they would enable the acquisition of the entire mid-IR spectra at each scan point. These developments are important as the future of IR-SNOM is in combining a SNOM instrument that performs with a nanometer resolution with a high-brightness (and affordable) mid-IR source.

References

- [1] R. M. Silverstein, G. C. Bassler, T. C. Morill, *Spectrometric Identification of Organic Compounds*, 5th edition, Wiley, New York (1991)
- [2] K. Nakanishi, *Infrared Absorption Spectroscopy - Practical*, Holden-Day Inc, San Francisco (1962)
- [3] Descriptions of several commercially available IR microscopes can be found at the following URLs:
http://www.jasco.co.uk/FTIR_microscope.asp,
<http://www.thermo.com/com/cda/product/detail/1,,20254,00.html>,
<http://las.perkinelmer.com/Catalog/ProductInfoPage.htm?ProductID=MULTISCP>
- [4] D. Naumann, D. Helm, H. Lebeschinski, *Nature* **351**, 81-82 (1991)
- [5] R. Mossadegh, J. S. Sanghera, D. T. Schaafsma, B. J. Cole, V. Q. Nguyen, R. E. Miklos, I. D. Aggarwal, *J. Lightwave Technol.* **16**, 214-217 (1998)
- [6] D. T. Schaafsma, R. Mossadegh, J. S. Sanghera, I. D. Aggarwal, M. Luce, R. Generosi, P. Perfetti, A. Cricenti, J. M. Gilligan, N. H. Tolk, *Opt. Eng.* **38**, 1381-1385 (1999)
- [7] D. B. Talley, L. B. Shaw, J. S. Sanghera, I. D. Aggarwal, A. Cricenti, R. Generosi, M. Luce, G. Margaritondo, J. M. Gilligan, N. H. Tolk, *Materials Letters* **42**, 339-344 (2000)
- [8] J. S. Sanghera, I. D. Aggarwal, *J. Non-Cryst. Solids* **256&257**, 6-16 (1999)
- [9] E. Betzig, J. K. Trautman, T. D. Harris, J. S. Weiner, and R. L. Kostelak, *Science* **251**, 1468-1470 (1991)
- [10] D. R. Turner, U.S. Patent No. 4,469,554 (1984)
- [11] R. Stöckle, C. Fokas, V. Deckert, R. Zenobi, B. Sick, B. Hecht, U. P. Wild, *Appl. Phys. Lett.* **75**, 160-162 (1999)
- [12] Amorphous Materials Inc, <http://www.amorphousmaterials.com/>
- [13] C. A. Brau, M. H. Mendenhall, *Proc. SPIE* **1854**, 2-10 (1993)
- [14] D. A. G. Deacon, L. R. Elias, J. M. J. Madey, G. J. Ramian, H. A. Schwettman, T. I. Smith, *Phys. Rev. Lett.* **38**, 892-894 (1977)

- [15] A. Cricenti, R. Generosi, C. Barchesi, M. Luce, M. Rinaldi, *Rev. Sci. Instrum.* **69**, 3240-3244 (1998)
- [16] Channel Industries Inc, Navy-c-5600 piezos
- [17] C. Barchesi, A. Cricenti, R. Generosi, C. Giammichele, M. Luce, M. Rinaldi, *Rev. Sci. Instrum.* **68**, 3799-3802 (1997)
- [18] Stanford Research Systems, Boxcar Averager SR250
<http://www.thinksrs.com/products/Boxcar.htm>
- [19] Electro - Optical Systems Inc, MCT14-020
http://www.eosystems.com/pdf/IS_MCT_cryo_detectors.pdf
- [20] J. D. Vincent, *Fundamentals of Infrared Detector Operation and Testing*, Wiley, New York (1990)
- [21] S. P. S. Arya, A. D'Amico, *Thin Solid Films* **157**, 267-282 (1988)
- [22] Sigma-Aldrich: 2, 4, 6 - Triethylborazine
- [23] R. M. Wentzcovitch, K. J. Chang, M. L. Cohen, *Phys. Rev. B* **34**, 1071-1079 (1986)
- [24] P. J. Gielisse, S. S. Mitra, J. N. Plendl, R. D. Griffis, L. C. Mansur, R. Marshall, E. A. Pascoe, *Phys. Rev.* **155**, 1039-1046 (1967)
- [25] I. Wegrzecka, M. Wegrzecki, M. Grynglas, J. Bar, A. Uszynski, R. Grodecki, P. Grabiec, S. Krzeminski, T. Budzynski, *Opto-Electron. Rev.* **12**, 95-104 (2004)
- [26] Jingze Tian, Lifang Xia, Xinxin Ma, Yue Sun, Eung-sun Byon, Sung-hun Lee, Sang-ro Lee, *Thin Solid Films* **355-356**, 229-232 (1999)
- [27] D. Vobornik, G. Margaritondo, P. Thielen, B. Ivanov, J. K. Miller, N. H. Tolk, A. Congiu-Castellano, et al., *Infrared Phys. Technol.* **45**, 409-416 (2004)
- [28] D. Vobornik, G. Margaritondo, J. S. Sanghera, P. Thielen, I. D. Aggarwal, B. Ivanov, N. H. Tolk, et al., *J. Alloy. Compd.* (2005), accepted for publication
- [29] U. M. Grassano, G. Margaritondo, R. Rosei, *Phys. Rev. B* **2**, 3319-3322 (1970)
- [30] R. M. Montereali, M. Piccinini, E. Burattini, *Appl. Phys. Lett.* **78**, 4082-4084 (2001)
- [31] K. Schwartz, C. Trautmann, T. Steckenreiter, O. Greiss, M. Kramer, *Phys. Rev. B* **58**, 11232-11240 (1998)
- [32] C. Vigreux, P. Loiseau, L. Binet, D. Gourier, *Phys. Rev. B* **61**, 8759-8770 (2000)

- [33] G. Baldacchini, F. Bonfigli, F. Flora, R. M. Montereali, D. Murra, E. Nichelatti, A. Faenov, T. Pikuz, *Appl. Phys. Lett.* **80**, 4810-4812 (2002)
- [34] G. Baldacchini, E. Burattini, L. Fornarini, A. Mancini, S. Martelli, R. M. Montereali, *Thin Solid Films* **330**, 67-69 (1998)
- [35] D. Attwood, *Soft X-rays and Extreme Ultraviolet Radiation: Principles and Applications*, Cambridge University Press (1999)
- [36] M. Montecchi, E. Nichelatti, A. Mancini, R. M. Montereali, *J. Appl. Phys.* **86**, 3745-3750 (1999)
- [37] G. Baldacchini, G. d'Auria, R. M. Montereali, A. Scacco, *J. Phys.: Condens. Matter* **10**, 857-867 (1998)
- [38] A. Cricenti, G. Longo, A. Ustione, V. Mussi, R. Generosi, M. Luce, M. Rinaldi, P. Perfetti, D. Vobornik, G. Margaritondo et al., *Appl. Surf. Sci.* **234**, 374-386 (2004)
- [39] M. Jackson, K. Kim, J. Tetteh, J. R. Mansfield, B. Dolenko, R. L. Somorjai, F. O. William, P. H. Watson, H. H. Mantsch, *SPIE* **3257**, 24-34 (1998)
- [40] H. H. Mantsch, D. Chapman (Eds.), *Infrared Spectroscopy of Biomolecules*, Wiley, New York (1996)
- [41] N. I. Afanasyeva, F. S. Kolyakov, S. G. Artjushenko, V. V. Sokolov, G. A. Franck, *SPIE* **3250**, 140-146 (1998)
- [42] B. Rigas, S. Morgello, I. S. Goldman, P. T. T. Wong, *Proc. Natl. Acad. Sci. USA* **87**, 8140-8144 (1990)
- [43] P. Lasch, D. Naumann, *Cell. Mol. Biol.* **44**, 189-202 (1998)
- [44] S. Mordechai, S. Argov, A. Salman, B. Cohen, R. Jagannathan, V. Erukhimovitch, J. Goldstein, I. Sinelnikov, *SPIE* **4129**, 231-242 (2000)
- [45] J. Ramesh, A. Salman, Z. Hammody, B. Cohen, J. Gopas, N. Grossman, S. Mordechai, *Eur. Biophys. J.* **30**, 250-255 (2001)
- [46] M. Diem, S. Boydston-White, L. Chiriboga, *Appl. Spectrosc.* **53**, 148-161 (1999)
- [47] P. Franck, P. Nabet, B. Dousset, *Cell. Mol. Biol.* **44**, 273-275 (1998)
- [48] A. Gaigneaux, C. Decaestecker, I. Camby, T. Mijatovic, R. Kiss, J. M. Ruysschaert, E. Goormaghtigh, *Exp. Cell Res.* **297**, 294-301 (2004)
- [49] G. L. Carr, M. Hanfland, G. P. Williams, *Rev. Sci. Instrum.* **66**, 1643-1645 (1995)

- [50] N. Jamin, P. Dumas, J. Moncuit, W.-H. Fridman, J.-L. Teillaud, G. L. Carr, G. P. Williams, *Proc. Natl. Acad. Sci. USA* **95**, 4837-4840 (1998)
- [51] H. Susi, D. M. Byler, *Methods Enzymol.* **130**, 290-311 (1986)
- [52] E. Goormaghtigh, V. Cabiaux, J.-M. Ruysschaert, *Determination of soluble and membrane protein structure by FT-IR: III. Secondary Structures*, in: H.J. Hilderson, G.B. Ralston (Eds.), *Subcellular Biochemistry*, Plenum, New York, 405– 450 (1994)
- [53] J. L. R. Arrondo, F. M. Goni, *Prog. Biophys. Mol. Biol.* **72**, 367–405 (1999)
- [54] C. P. Schultz, K. Z. Liu, J. B. Johnston, H. H. Mantsch, *Leukemia Res.* **20**, 649–655 (1996)
- [55] P. T. T. Wong, M. Codrin, S. W. French, *Exp. Mol. Pathol.* **55**, 269–284 (1991)
- [56] A. Cricenti, R. Generosi, M. Luce, P. Perfetti, G. Margaritondo, D. Talley, J. S. Sanghera, I. D. Aggarwal, N. H. Tolk, et al., *Biophysical J.* **85**, 2705-2710 (2003)
- [57] J. H. van der Maas, *Basic Infrared Spectroscopy*, 2nd Ed. Heyden & Son Ltd., London, UK (88-89)
- [58] K. Simons, E. Ikonen, *Nature* **387**, 569-572 (1997); R. G. W. Andersen, K. Jacobson, *Science* **296**, 1821-1825 (2002); M. Edidin, *Annu. Rev. Biophys. Biomol. Struct.* **32**, 257-283 (2003)
- [59] P. Burgos, C. Yuan, M.-L. Viriot, L. J. Johnston, *Langmuir* **19**, 8002-8009 (2003)
- [60] M. Diem, S. Boydston-White, L. Chiriboga, *Appl. Spectrosc.* **53(4)**, 148-161 (1999)
- [61] O. Sqalli, M.-P. Bernal, P. Hoffmann, F. Marquis-Weible, *Appl. Phys. Lett.* **76**, 2134-2136 (2000)
- [62] H. G. Frey, S. Witt, K. Felderer, R. Guckenberger, *Phys. Rev. Lett.* **93**, 200801 (2004)
- [63] A. Piednoir, C. Licoppe, F. Creuzet, *Opt. Commun.* **129**, 414-422 (1996)
- [64] M. K. Hong, A. G. Jeung, N. V. Dokholyan, T. I. Smith, H. A. Schwettman, P. Huie, S. Erramilli, *Nucl. Instr. and Meth. in Phys. Res. B* **144**, 246-255 (1998)
- [65] C. A. Michaels, S. J. Stranick, L. J. Richter, R. R. Cavanagh, *J. Appl. Phys.* **88**, 4832-4839 (2000)
- [66] B. Dragnea, J. Preusser, W. Schade, S.R. Leone, *J. Appl. Phys.* **86**, 2795-2799 (1999)

-
- [67] B. Dragnea, J. Preusser, J.M. Szarko, L.A. McDonough, S.R. Leone, W.D. Hinsberg, *Appl. Surf. Sci.* **175-176**, 783-789 (2001)
- [68] B. Knoll, F. Keilmann, *Nature* **399**, 134-137 (1999)
- [69] B. B. Akhremitchev, Y. Sun, L. Stebounova, G. C. Walker, *Langmuir* **18**, 5325-5328 (2002)
- [70] G. van Meer, R. M. J. Liskamp, *Nature Methods* **2**, 14-15 (2005)

3 Fluorescence SNOM Imaging

A new scanning near-field microscopy instrument was built at EPFL. Now fully operational, the instrument is used for experiments that are complementary to the aforementioned IR-SNOM experiments. Specifically, the new SNOM is dedicated primarily to the study of fluorescently marked structures. The main instrumental components of the SNOM are briefly described, as well as the ongoing experiments, which show the high quality and experimental possibilities of this SNOM system. Finally, SNOM images of fluorescently labeled cells and carbon nanotubes are presented and analyzed.

3.1 *Introduction*

The fluorescence microscopy has become one of the most important research tools in modern cell biology [1]. This has encouraged the development of an ever-growing variety of sophisticated fluorescent probes that can be attached with high selectivity

to the chemicals of interest [2]. Fluorescent microscopy thereby offers a highly selective contrast. It is non-destructive and can be used to image living cells. The advent of green fluorescent protein (GFP) technology has further revolutionized fluorescent live cell imaging by allowing an auto-fluorescent protein to be genetically encoded through a fusion of the GFP gene with the genes that encode the cell structures of interest [3]. A wide range of detectors, such as avalanche photodiodes, photomultiplier tubes, CCD cameras and photon counting devices, that enable optical detection down to the single molecule level, are available for fluorescent microscopy applications. All this ensures a prominent role for fluorescence microscopy in the future.

Confocal microscopy dominates fluorescence imaging today. However, other techniques, such as SNOM, multi-photon and total internal reflection fluorescence, are gaining interest because of the increased resolution that they offer.

The illumination of fluorophores causes photo-bleaching. The light emitted through an aperture whose diameter is much smaller than the wavelength is an evanescent non-propagating light (Chapter 1, section 1.4.4). The aperture-based SNOM probe thereby illuminates and excites fluorescence only in the layer that is less than 100 nm from the aperture. This extremely small near-field excitation volume makes aperture-based SNOM extremely interesting for fluorescence imaging. The small excitation volume offers several benefits all at once: an increased fluorescence resolution, greatly reduced photo-bleaching and no background fluorescence.

Since it combines topographical information, optical super-resolution and a demonstrated single molecule detection sensitivity [4], SNOM is a unique tool for biological applications. This has already led to a certain development of fluorescence SNOM bio-imaging [4-9], as well as to the development of a fluorescence SNOM setup at EPFL.

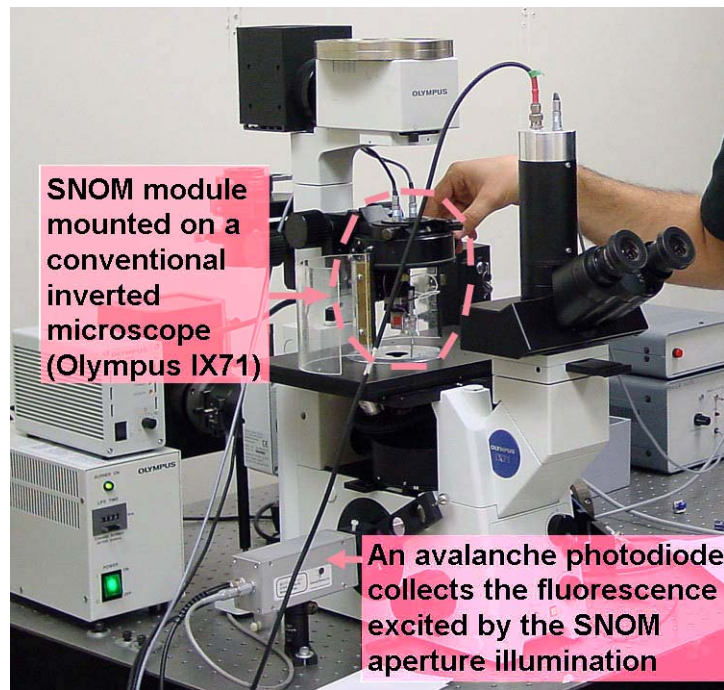


Figure 3-1: Fluorescence SNOM experimental setup at EPFL

3.2 Experimental Setup

The experimental setup consists of a homemade SNOM scanning module mounted on a conventional inverted microscope [10] (figure 3-1).

There are several reasons for combining a conventional microscope with a SNOM instrument. The conventional microscope can be used to select the part of the sample that is of interest, and to position it easily and quickly under the SNOM aperture before initiating the scan. With a camera mounted onto the microscope, the image can first be recorded with the conventional microscope, and then with SNOM; a comparison of the two images is often critical for a better understanding of the SNOM results. The high numerical aperture oil immersion objective of the conventional microscope can be used for a highly efficient collection of the SNOM fluorescence and for focusing the signal onto an avalanche photodiode.

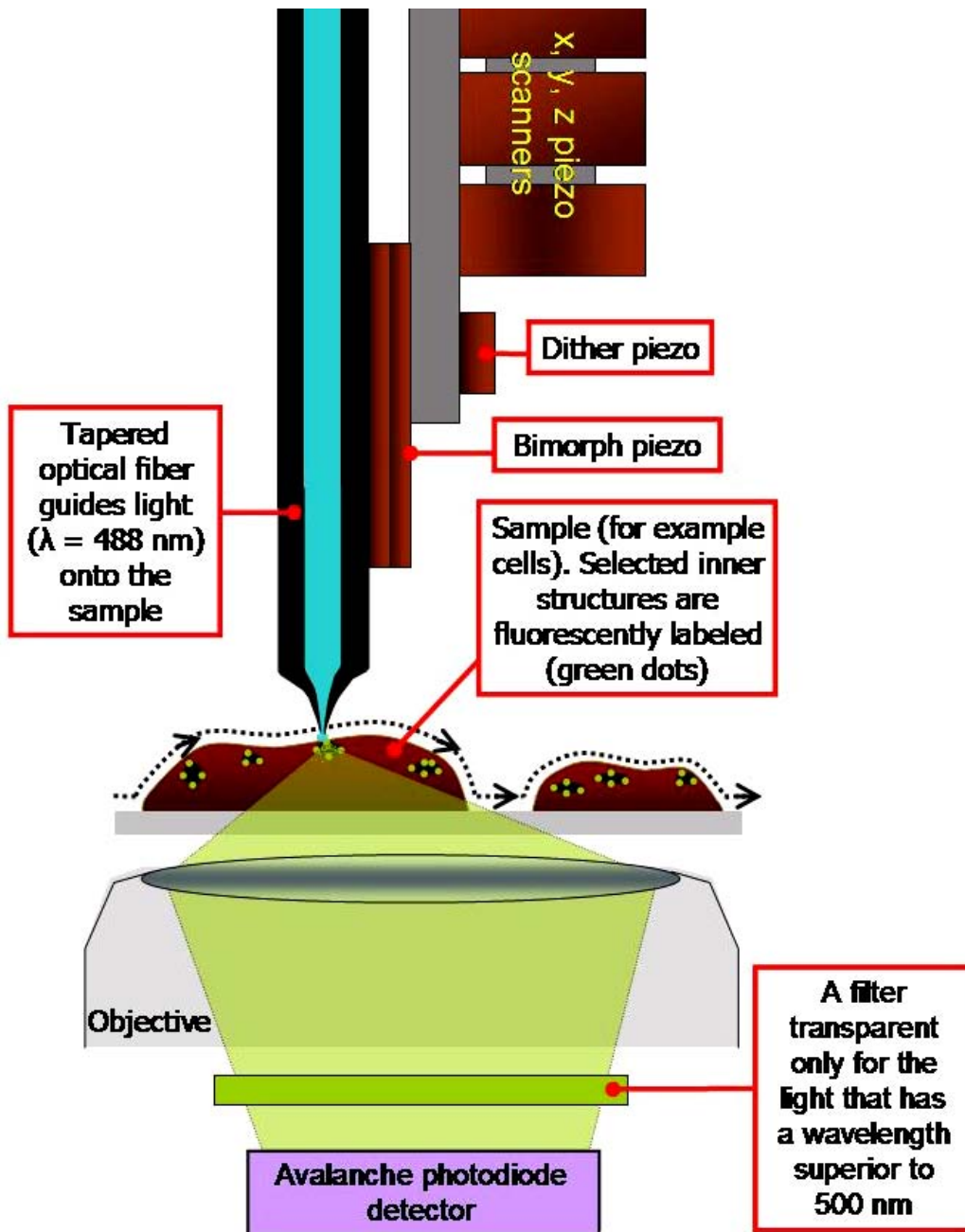


Figure 3-2: Fluorescence SNOM experimental scheme.

This instrumental setup is operated in the illumination mode (figure 3-2): the laser [11] beam is coupled into the fiber and guided onto the sample surface. It illuminates the sample through a sub-wavelength-sized aperture. If a fluorophore is less than $\sim 100 \text{ nm}$ from the aperture, its fluorescence emission is excited, collected by the objective and detected by an avalanche photodiode detector [12].

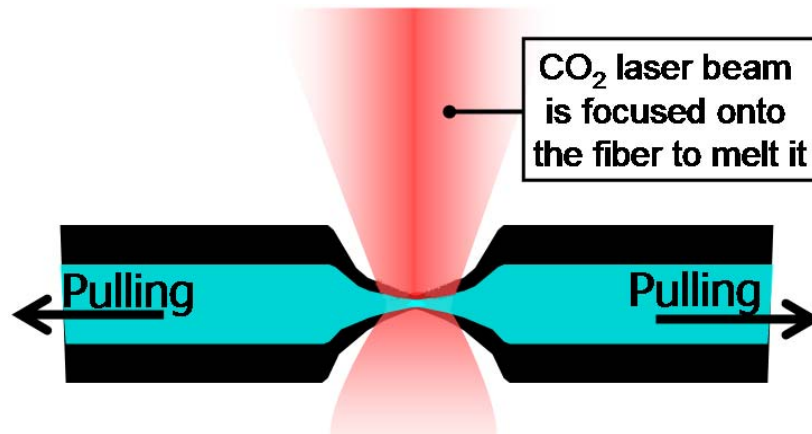


Figure 3-3: Fiber tips were fabricated using a heating-and-pulling method

Since the setup works with visible light, standard telecommunication silica optical fibers with 8 μm core diameters were used. Fiber tapering is one of the most critical steps for successful SNOM imaging. A micropipette puller (Sutter Co. P2000) was used to taper fiber tips: it simultaneously pulls and melts the optical fiber (figure 3-3). The shape of the fiber tips can be modified by adjusting the pulling and the CO₂ laser beam intensities.

In this setup, the SNOM fiber is attached to the scanner (figure 3-3). The maximal scan range of the scanner [13] is 40 μm \times 40 μm in the x - y plane and 8 μm in the z direction, with a nominal resolution of 0.07 nm in the x - y plane, and 0.01 nm along the z axis. The electronics used in this setup are the same as the ones described in section 2.3.5 of Chapter 2.

3.3 Imaging of Fluorescently Labeled Cells

Figure 3-4 shows SNOM images of a fibroblast cell (which belongs to the COS-9 cell line). Such cells were seeded on glass slides, and fixed in paraformaldehyde after 10 minutes of internalization of fluorescein-conjugated wheat germ agglutinin (WGA-FITC).

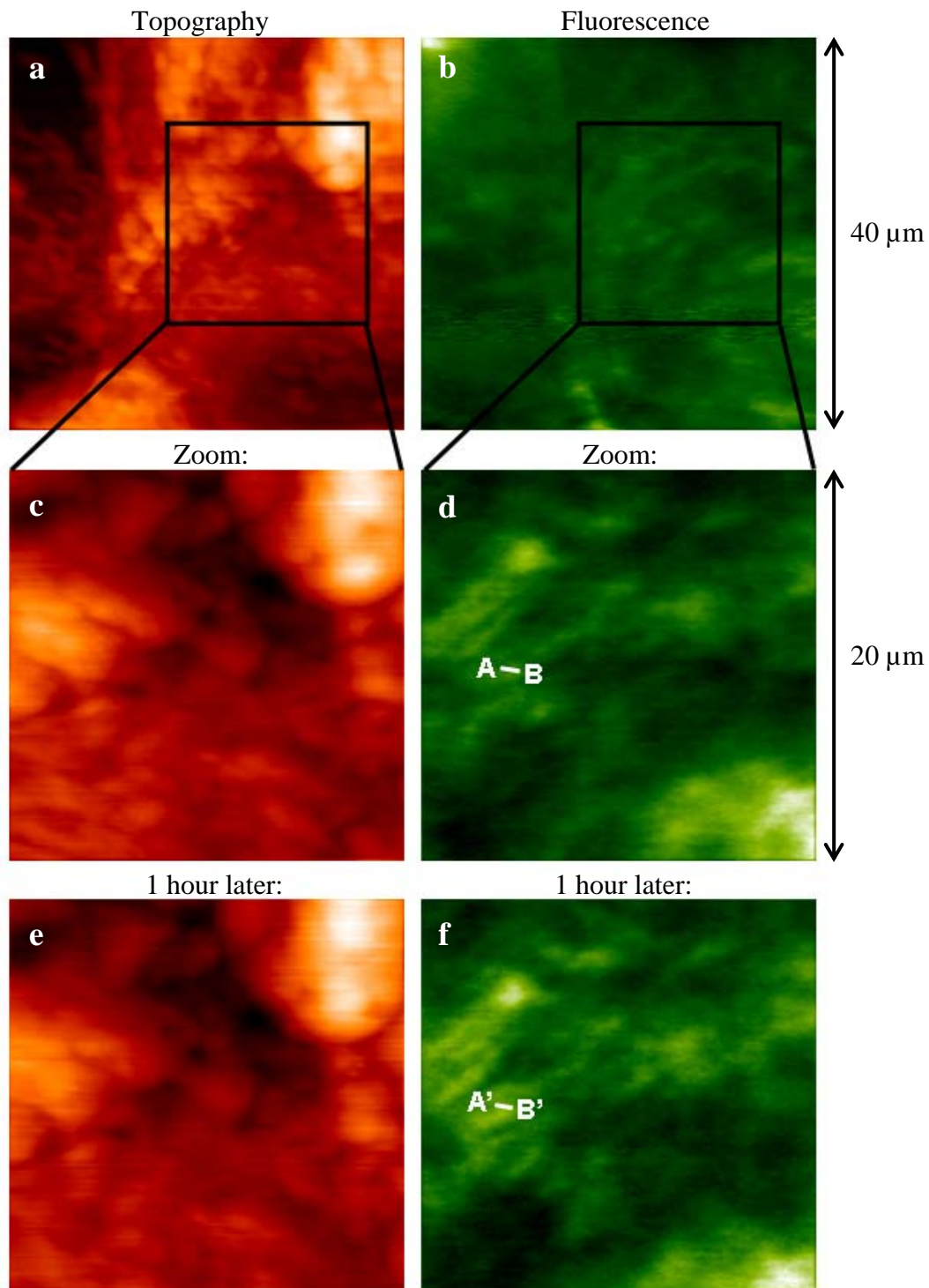


Figure 3-4: SNOM images of fibroblast cells (COS-9 cell line). Topography is shown in red (a, c and e) and the corresponding fluorescence in green (b, d and f); c, d e and f are zoom images of the area inside the square in a and b; e and f were acquired one hour after c and d.

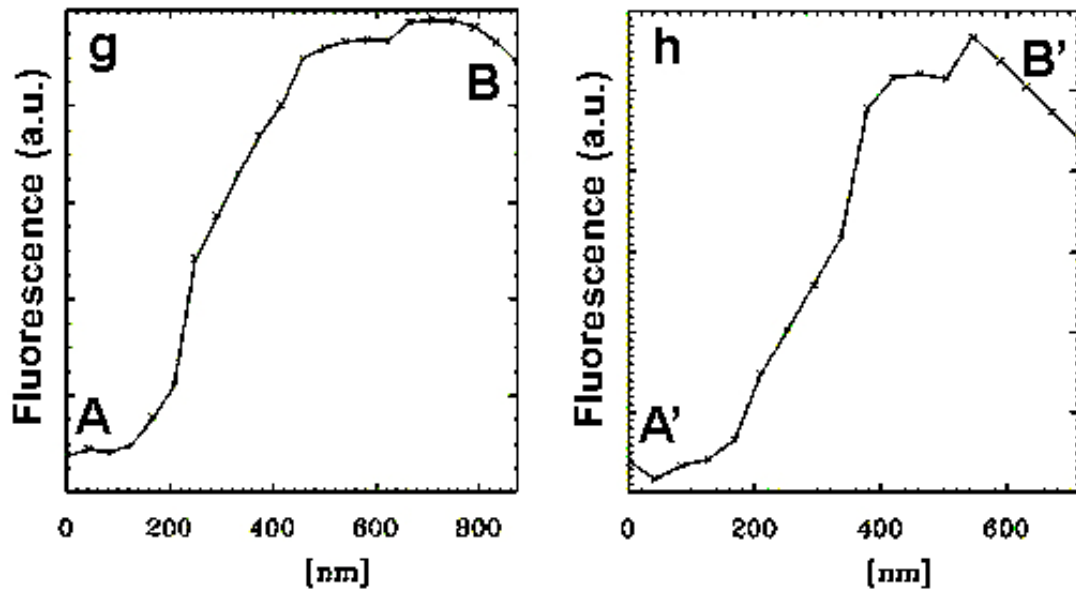


Figure 3-5: (g) is a cross-section that corresponds to the line A-B of figure 3-4d, and (h) is a cross-section that corresponds to the line A'-B' of figure 3-4f.

WGA-FITC is a fluorophore that is excited by the 488 nm line of an argon ion laser, while its fluorescence emission maximum is at 530 nm.

Topography and fluorescence images in figures 3-4a and b were acquired simultaneously. These $40\ \mu\text{m} \times 40\ \mu\text{m}$ images show a part of a fibroblast cell. The topographically highest zone, which can be seen in the upper right corner of figure 3-4a, corresponds to the cell nucleus. Figures 3-4c and d were acquired over the zone that corresponds to the square drawn in both 3-4a and b. These are $20\ \mu\text{m} \times 20\ \mu\text{m}$ images that were acquired with 300 acquisition points per line. The scan was completed in approximately 35 minutes. In order to test the stability of the setup and the incidence of SNOM-induced photo-bleaching, an identical scan was performed one hour later. The resulting images are shown in figures 3-4e and f. Figures 3-5g and h show cross-sections corresponding to the lines A-B in figure 3-4d and A'-B' in figure 3-4f.

Images shown in figure 3-4 are results of the first series of tests that were conducted with the fluorescence SNOM instrument. A comparison of figures 3-4c and 3-4e demonstrates the good overall stability of the instrument. Acquired with a time

interval of one hour, the two figures are essentially identical. Figures 3-4d and 3-4f do not reveal any considerable differences either, and therefore indicate that any SNOM-induced photo-bleaching can be neglected. Figures 3-5g and 3-5h show the cross-sections that correspond to the same part of the fluorescence images 3-4d and 3-4f. They show the same overall shape, and therefore demonstrate once more the good stability of the SNOM instrument and the absence of any contrast loss, an issue that could be problematic in conventional or scanning confocal microscopy.

In all three fluorescence images (figures 3-4b, c and d) tubular shapes can clearly be identified; these correspond to endosomes, which are cellular organelles that are inside the cells, not in their membranes. The resolution can be assessed from the cross-sections shown in figure 3-5: its value is of the order of 200 nm. Since the stained endosomes are inside the cells, relatively far from the surface, this result demonstrates that SNOM can also be used for sub-diffraction imaging of inner cellular structures, and not only for the imaging of cell surface structures. The resolution is somewhat lower when imaging surface structures (200 nm instead of 100 nm), but still superior to the resolution of conventional microscopes.

3.4 Carbon Nanotubes Fluorescence Imaging

3.4.1 Introduction

Promising applications of carbon nanotubes range from nanoscale devices and materials [14] to field emission [15] and scanning probe microscopy [16]. However, the difficulties encountered in the synthesis of high quality nanotubes are a serious limiting factor. Carbon nanotubes are typically produced by an arc-discharge method [17], with a wide distribution of lengths and diameters. Nanoparticles consisting of graphitic layers of polyhedral shape make up to one half of the weight of the nanomaterial deposit. A popular purification method uses a water/surfactant solution

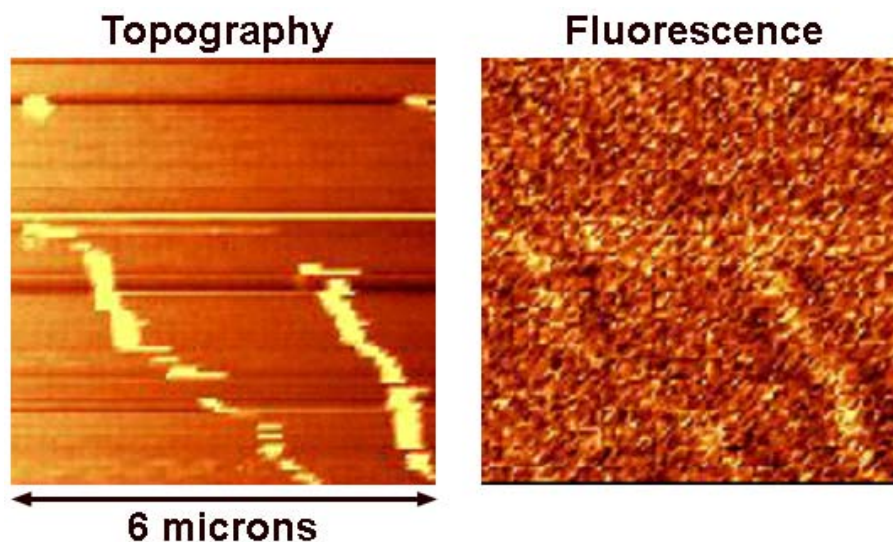


Figure 3-6: SNOM images of fluorescently labeled carbon nanotubes

to purify arc-discharge-produced nanotubes [18]. The surfactant most-commonly used in this procedure is sodium dodecylsulfate (SDS). Surfactants constitute the most important group of detergent components. Generally, these are water-soluble surface-active agents that are comprised of a hydrophobic portion, usually a long alkyl chain attached to hydrophilic or water solubility-enhancing functional groups. Recently, electron microscopy images suggested that SDS might attach to the surface of nanotubes' [19] and stay bound there after the purification process. This could have important consequences on nanotube conductivity, solubility and chemical reactivity. Previous reported measurements of these nanotube properties would have to be reanalyzed in order to verify whether the properties correspond to the nanotubes or to the SDS attached to their surface.

3.4.2 Experiment

To verify if some of the SDS stay attached to the nanotubes after the purification process, a fluorescent probe [20] that chemically mimics SDS was added to the water/surfactant solution. The nanotubes' post-purification solution composition was: 100 ml of H₂O, 5 mg of multi-walled, arc-discharge-produced nanotubes, 20 mg of SDS and 2 mg of 5-dodecanoylamino fluorescein fluorophore. The 5-

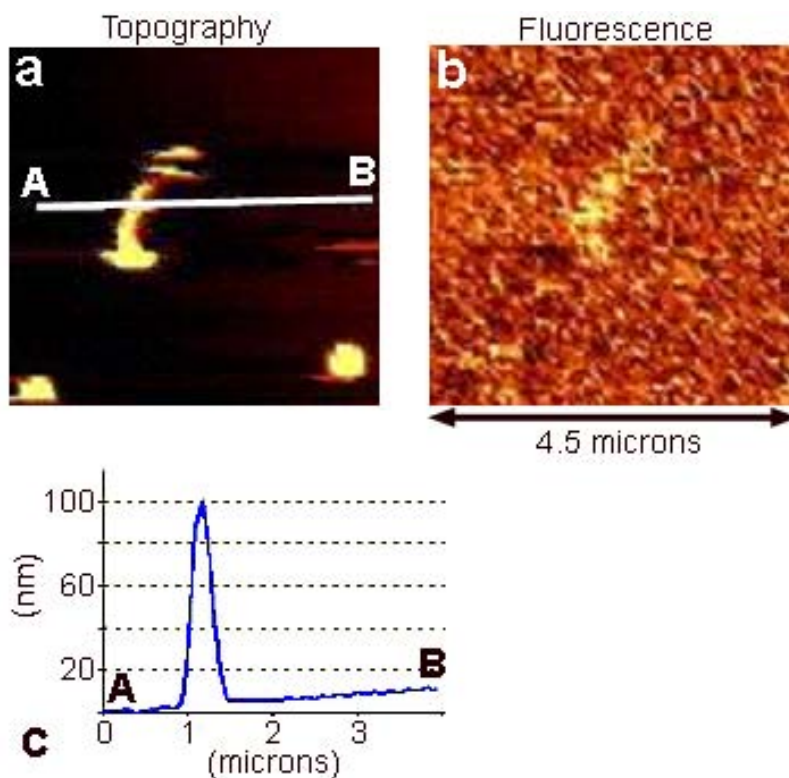


Figure 3-7: SNOM imaging of fluorescently labeled nanotubes. (a) SNOM topography; (b) SNOM fluorescence image; (c) topographic cross-section that corresponds to the line A-B in 3-7a

dodecanoylamino fluorescein fluorophore has a chemical structure that is very similar to SDS, and is expected to undergo the same chemical reactions as the SDS when put in the same conditions. In other words, if SDS really stays bonded to nanotubes after the purification, 5-dodecanoylamino fluorescein should also remain bonded. Since this molecule is fluorescent, it provides a strong contrast for SNOM imaging. A few droplets of the nanotube solution were deposited on a glass slide and left to dry. The glass slide was then put in the SNOM instrument and scanned. Figures 3-6 and 3-7 show the corresponding results. Figure 3-6 shows a $6\ \mu\text{m} \times 6\ \mu\text{m}$ image. Two nanotubes can be seen in both the topographic and fluorescence images. Fluorescence images, although quite noisy, clearly indicate that there is a fluorescence emission arising from the nanotubes.

This optical signal may at first seem to be a topography-induced artifact. However, it is proven otherwise. The images shown here were scanned over the zones where the

nanotubes are in close proximity of amorphous carbon heaps. In figure 3-6 such a heap can be seen in the upper left corner of the topographic image. Yet, it does not produce any contrast in the fluorescence image. If the fluorescence of the nanotubes was a consequence of topographic artifacts, the amorphous carbon heap would have produced the same kind of contrast, since it has the same topographic cross-section.

Figure 3-7a shows one nanotube and two amorphous carbon heaps in the lower right and left corners. Again, there is no noticeable contrast arising from the heaps in the fluorescence image. The height of the nanotube can be estimated from the cross-section in figure 3-7c. According to the cross-section, the nanotubes' FWHM is of the order of 250 nm. However, this value most likely corresponds to the diameter of the SNOM probe tip – with scanning probe microscopes, if the probe size is bigger than the sample size, it is not the probe that images the sample, but the sample that images the probe. We can still estimate the diameter of the nanotube from the height given in the cross-section, which is around 100 nm. This is consistent with the electron microscopy observations of the nanotubes: statistically, their diameters were found to form a Gaussian distribution centered at around 80 nm.

3.5 Conclusion

The SNOM images that are shown in this chapter are the first results obtained with the new SNOM setup at EPFL. The setup combines high quality conventional optics with a standard aperture-based SNOM instrument. It also includes an Argon ion laser, fluorescence filters, and a high sensitivity avalanche photo diode, which together enable fluorescence measurements. In this thesis, two fluorescence SNOM applications have been presented: the imaging of fluorescently labeled cells as well as the imaging of carbon nanotubes. Cell experiments demonstrated the good mechanical stability of the instrument and its suitability for fluorescence measurements when photo-bleaching is problematic. Still in the experimental stage of its development, the fluorescence SNOM instrument has already produced very

interesting results with carbon nanotubes. These preliminary results show that there is an amount of SDS that remains attached to nanotubes as a result of the purification procedure. The results demonstrate that SNOM can be used to image sub-100 nm-sized objects. The most exciting development of fluorescence SNOM is the possibility of studying soft and motile living cells in physiological conditions, where innovative SNOM designs that operate in the tapping scanning mode have started delivering promising results [9].

References

- [1] D. J. Stephens, V. J. Allan, *Science* **300**, 82-86 (2003)
- [2] Invitrogen Corporation is one of the leaders of the fluorophore market. A lot of information about their products is available at the following URL:
<http://probes.invitrogen.com/>
- [3] J. Lippincott-Schwartz, G. H. Patterson, *Science* **300**, 87-91 (2003)
- [4] E. Betzig, R. J. Chichester, *Science* **262**, 1422-1425 (1993)
- [5] E. Betzig, R. J. Chichester, F. Lanni, D. L. Taylor, *Bioimaging* **1**, 129-133 (1993)
- [6] T. Enderle, T. Ha, D. F. Ogletree, D. S. Chemla, C. Magowan, S. Weiss, *Proc. Natl. Acad. Sci. USA* **94**, 520-525 (1997)
- [7] M. F. Garcia-Parajo, J. A. Veerman, A. G. Ruitter, N. F. Van Hulst, *Ultramicroscopy* **71**, 311-319 (1998)
- [8] M. F. Garcia-Parajo, G. M. Segers-Nolten, J. A. Veerman, J. Greve, N. F. Van Hulst, *Proc. Natl. Acad. Sci. USA* **97**, 7237-7242 (2000)
- [9] A. Ianoul, M. Street, D. Grant, J. Pezacki, R. S. Taylor, L. J. Johnston, *Biophys. J.* **87**, 3525-3535 (2004)
- [10] Olympus IX71 information available at the following URL:
http://www.olympus-europa.com/medical/22_IX71.htm
- [11] Argon ion laser, purchased from LG-Laser Technologies GmbH, model 165LGA. Information available at the following URL:
http://www.lg-lasertechnologies.com/en/produkte/argon/165lg_serie.html
- [12] Avalanche photo diode model 394-70-74-661 purchased from Advanced Photonix Inc. Information available at the following URL:
http://www.advancedphotonix.com/pdf/oem_modules_cooled.pdf
- [13] Piezosystem jena GmbH, scanners series: PXY 38 and PZ 8 D 12
- [14] M. M. J. Treacy, T. W. Ebbesen, J. M. Gibson, *Nature* **381**, 678-680 (1996)
- [15] W. A. de Heer, A. Châtelain, D. Ugarte, *Science* **270**, 1179-1180 (1995)
- [16] H. J. Dai, J. H. Hafner, A. G. Rinzler, D. T. Colbert, R. E. Smalley, *Nature* **384**, 147-150 (1996)
- [17] S. Iijima, *Nature* **354**, 56-58 (1991)

- [18] J.-M. Bonard, T. Stora, J.-P. Salvetat, F. Maier, T. Stockli, C. Duschl, L. Forro, W. A. De Heer, A. Chatelain, *Adv. Mater.* **9**, 827 (1997)
- [19] C. Richard, F. Balavoine, P. Schultz, T. W. Ebbesen, C. Mioskowski, *Science* **300**, 775-778 (2003)
- [20] 5-dodecanoylamino fluorescein purchased from Invitrogen (catalogue number D 109)

Conclusion

The spectroscopic IR-SNOM combines the IR spectroscopy's high chemical specificity with the SNOM's high optical and topographical resolutions. The IR-SNOM experiments described in this thesis demonstrate that it is an extremely powerful analytical technique.

Presented in this work are IR-SNOM images with a 100 nm resolution. This resolution corresponds to a value of $\lambda/60$ (where λ is the illumination wavelength), which is more than 30 times better than the best possible resolution that can be achieved with lens-based microscopes.

Comparisons between IR-SNOM topographic and spectroscopic images enabled a clear characterization and understanding of the structure of LCVD grown BN films. Even a combination of several other research techniques could hardly give such an accurate description of this kind of sample, which is both highly granular and chemically heterogeneous.

It was demonstrated in this thesis that the IR-SNOM technique is applicable to biological samples. Infrared spectroscopic cell imaging is probably the most exciting SNOM application presented. The resolution achieved when imaging cells was the same as the one achieved when imaging materials science samples. The images presented are unique because of their high 100 nm resolution, but also because they are the first IR images that show resolved inner cellular structures. The lipid raft imaging demonstrates that the IR-SNOM can tackle the hottest research topics today. Furthermore, IR-SNOM offers a unique, non-invasive way of imaging, where the contrast agents and dyes that dominate bio-imaging today, and which are known to modify the structure and behavior of the imaged constituents, are no longer required.

The fluorescence SNOM images shown in this thesis are the first results obtained with the newly built SNOM setup at EPFL. The setup combines high quality conventional optics with a standard aperture-based SNOM instrument. Two fluorescence SNOM experiments are presented: the imaging of fluorescently labeled cells and the imaging of carbon nanotubes. The cell experiments demonstrate the good mechanical stability of the instrument and its suitability for fluorescence measurements of biological samples, particularly when photo-bleaching is a problematic issue, which is often the case with conventional microscopy. The fluorescence SNOM instrument has produced very interesting results with carbon nanotubes. These results show that a widely used nanotube purification procedure needs further improvement because some of the purification surfactant remains attached to nanotubes.

Today, SNOM is a mature tool, ready for applications both in materials science and in bio-medical research. Further developments of the apertureless SNOM and of the IR sources could soon transform the IR-SNOM into a widely used and even more potent instrument. The development of the apertureless SNOM technique could further increase the resolution by more than an order of magnitude to achieve 10 nm (or less)-scale imaging. More closely related to the IR spectroscopic capabilities is the development of table-top high-brightness IR sources that would cover the whole mid-IR spectral range, thus replacing more expensive free electron laser sources and making IR-SNOM more widely available. As for the fluorescence SNOM, the most exciting development is the possibility of studying soft and motile living cells in physiological conditions, where innovative SNOM designs that operate in the tapping scanning mode have started delivering promising results.

Acknowledgments

I am indebted to many great people that have worked with me, given me support and helped me along the way.

First of all, I thank Prof. Giorgio Margaritondo, who provided me with his full support and helped me whenever I asked for assistance, no matter how busy he was. He trusted me and gave me a lot of autonomy, but also the responsibilities that come with such independence, and thus offered me one of the best possible preparations for my future scientific career.

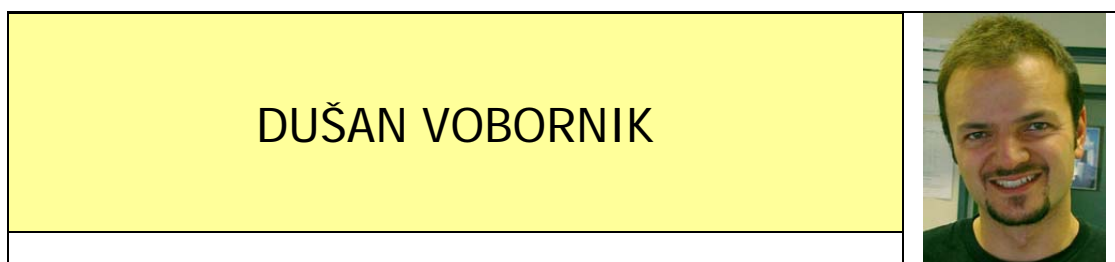
Profound thanks go to Prof. Antonio Cricenti, Renato Generosi, Marco Luce, Marco Girasole and to all the other collaborators from the Istituto di Struttura della Materia in Rome, Italy. They taught me all the finer details of scanning probe microscopy. They were always there to rescue me when I would break some piece of my SNOM instrumentation. I will fondly remember the time we spent together in the “cantinas” of Frascati in Rome, as well as Antonio’s pasta “aglio-olio-peperoncino” at FEL. I would like to thank all my collaborators at Vanderbilt University in Nashville, Tennessee, and in particular Prof. Norman Tolk, Prof. David Piston, Borislav Ivanov, Andrey Zavalin, John Kozub and all the FEL staff without whom this work would not have been possible. I would also like to thank all my collaborators at EPFL, particularly Pascal Steiner, Michel Kropf and Harald Hirling who enthusiastically prepared cell samples for me, as well as the technicians of IPMC who built several essential pieces of the SNOM experimental setup at EPFL.

Very special thanks go to Professors Davor Pavuna and Laszlo Forró of EPFL. Davor’s open-minded and refreshing approach to science and life and his wise advice enriched me a lot.

I would like to thank all my EPFL friends. Daniel Ariosa made me laugh so many times with his excellent jokes. The way Daniel enjoys his work and science has set a great example for me. Claudia Cancellieri, Amela Groso, Dominique Cloetta and Marco Papagno have been perfect office-mates, and were often able to transform the greyest Lausanne days into warm and sunny moments. Slobodan Mitrovic, Branimir Lukic, Iva Tkalcec and Camilo Guzman read large parts of this thesis and gave me valuable feedback, and also many moments of laughter and friendship. Very special thanks go to Katarina Blagovic and Ivica Stevanovic, my Saturday coffee, cinema and hiking partners and friends who gave me precious advice concerning the writing of this thesis. Thanks also go to all the other people from EPFL (I am surely forgetting many) who contributed to making my life in Lausanne pleasant and joyful.

A huge “thank you” goes to Joanne LaBossière who, with incredible patience and kindness, read this whole thesis and transformed my often chaotic ideas into sense-full sentences.

Finally, I would like to express my love and gratitude to all my family for their unconditional support and encouragement.



<i>Address:</i> Chemin de Croset 8 1024 Ecublens, Switzerland <i>Phone:</i> + 41 21 693 54 22 <i>Fax:</i> + 41 21 693 46 66	Born on June 20, 1976 Citizen of Croatia
	E-mail: dusan.vobornik@epfl.ch Web page: https://nanotubes.epfl.ch/lprx/2/DusanCV.htm

ACADEMIC BACKGROUND

- 2001-2005 PhD in Physics**
 Subject: Scanning Near-field Optical Microscopy
 Ecole Polytechnique Fédérale de Lausanne (EPFL), Lausanne, Switzerland
- 1999-2001 Master's Degree in Microelectronics**
Diplôme d'Etudes Approfondies (DEA) en Microélectronique,
 Université Joseph Fourier, Grenoble, France
- 1996-1999 Bachelor's Degree in Physics**
Licence de Physique
 Université Joseph Fourier, Grenoble, France

PROFESSIONAL EXPERIENCE

Research and Teaching Assistant

Institute of Physics of the Complex Matter, EPFL, Switzerland
Thesis director: Prof. G. Margaritondo

- Measure and analyze biological and material science samples with Scanning Near-Field Optical Microscopy (SNOM); improve and develop SNOM instruments for imaging of biological samples; perform infrared SNOM (IR-SNOM) experiments with the Free Electron Laser (FEL) light source (Vanderbilt University FEL, Nashville, Tennessee)
- Prepare and supervise exercises in mechanics, thermodynamics, electromagnetism, optics and quantum mechanics for first and second year students at EPFL

Research Assistant- Internship

Institute of Applied Physics, EPFL, Lausanne, Switzerland

Internship supervisor: Prof. D. Pavuna

- Fabricated superconducting thin films (LSCO, YBCO, BSCCO) using the Pulsed Laser Deposition (PLD) technique
- Analyzed films with the photoemission technique at the Synchrotron Radiation Center in Madison, WI, USA

Research Assistant- Internship

LEPES-CNRS Laboratory, Grenoble, France

Internship supervisor: E. Bustarret

- Studied the role of mechanical strain in thin films of epitaxially grown SiC and GaN using the Raman Spectroscopy technique.

SPECIFIC QUALIFICATIONS

- **Languages written and spoken:** English, French and Croatian
Basic knowledge of Italian
- **Computer knowledge:** - All standard PC and Mac hardware and software
 - Programming (C, C++, Pascal)
 - Web design

OTHER INTERESTS

- **Sports:** cycling, skiing, in-line skating, basketball, outdoor activities
- **Music:** play piano and guitar
- **Traveling**

PUBLICATIONS

1- **Spectroscopic Infrared Scanning Near-field Optical Microscopy (IR-SNOM)**
D. Vobornik, G. Margaritondo, J. S. Sanghera, P. Thielen, I. D. Aggarwal, B. Ivanov, et al., Accepted for publication, JOURNAL OF ALLOYS AND COMPOUNDS, (2005)

2- Infrared Near-field Microscopy with the Vanderbilt Free Electron Laser: Overview and Perspectives

D. Vobornik, G. Margaritondo, P. Thielen, B. Ivanov, J. K. Miller, N. H. Tolk, et al., INFRARED PHYSICS & TECHNOLOGY 45 (5-6): 409–416 (2004)

3- Optical Nanospectroscopy Applications in Material Science

A. Cricenti, G. Longo, A. Ustione, V. Mussi, R. Generosi, M. Luce, M. Rinaldi, P. Perfetti, D. Vobornik et al., APPLIED SURFACE SCIENCE 234 (1-4): 374-386 (2004)

4- Direct Photoemission Spectroscopy and Electronic Properties of In-situ Grown, Strained High-Tc and Related Oxide Films

M. Abrecht, D. Ariosa, D. Cloëtta, D. Vobornik, G. Margaritondo, D. Pavuna JOURNAL OF PHYSICS AND CHEMISTRY OF SOLIDS 65 (8-9): 1391-1395 (2004)

5- Optical Nanospectroscopy Study of Ion-implanted Silicon and Biological Growth Medium

A. Cricenti, V. Marocchi, R. Generosi, M. Luce, P. Perfetti, D. Vobornik, G. Margaritondo, et al., JOURNAL OF ALLOYS AND COMPOUNDS, 362 (1-2): 21-25 (2004)

6- IR-SNOM on Lithium Fluoride Films with Regular Arrays Based on Color Centers

A. Cricenti, G. Longo, V. Mussi, R. Generosi, M. Luce, P. Perfetti, D. Vobornik, G. Margaritondo, et al., PHYSICA STATUS SOLIDI C, 0 (8): 3075-3080 (2003)

7- AFM and SNOM Characterization of Carboxylic Acid Terminated Silicon and Silicon Nitride Surfaces

A. Cricenti, G. Longo, M. Luce, R. Generosi, P. Perfetti, D. Vobornik, G. Margaritondo, P. Thielen, et al., SURFACE SCIENCE, 544 (1): 51-57 (2003)

8- Interfacial Strain in 3C-SiC/Si(100) Pseudo-substrates for Cubic Nitride Epitaxy

E. Bustarret, D. Vobornik, A. Roulot, T. Chassagne, G. Ferro, Y. Monteil, E. Martinez-Guerrero, et al., PHYSICA STATUS SOLIDI A, 195 (1): 18-25 (2003)